Geophysical Journal International

Geophys. J. Int. (2014) **196,** 253–278
Advance Access publication 2013 October 16

doi: 10.1093/gji/ggt343

On precisely modelling surface deformation due to interacting magma chambers and dykes

Karen Pascal,[1,2] Jurgen Neuberg[1] and Eleonora Rivalta[3,4]

[1] *School of Earth & Environment, University of Leeds, Leeds LS2 9JT, United Kingdom. E-mail: PascalK@mvo.ms*
[2] *Montserrat Volcano Observatory, Flemmings, Montserrat, West Indies*
[3] *Institute of Geophysics, University of Hamburg, Bundesstr. 55, D-20146 Hamburg, Germany*
[4] *GFZ Potsdam, Helmholtzstrasse 7, D-14467 Potsdam, Germany*

Accepted 2013 August 28. Received 2013 June 2; in original form 2012 June 25

SUMMARY

Combined data sets of InSAR and GPS allow us to observe surface deformation in volcanic settings. However, at the vast majority of volcanoes, a detailed 3-D structure that could guide the modelling of deformation sources is not available, due to the lack of tomography studies, for example. Therefore, volcano ground deformation due to magma movement in the subsurface is commonly modelled using simple point (Mogi) or dislocation (Okada) sources, embedded in a homogeneous, isotropic and elastic half-space. When data sets are too complex to be explained by a single deformation source, the magmatic system is often represented by a combination of these sources and their displacements fields are simply summed. By doing so, the assumption of homogeneity in the half-space is violated and the resulting interaction between sources is neglected. We have quantified the errors of such a simplification and investigated the limits in which the combination of analytical sources is justified. We have calculated the vertical and horizontal displacements for analytical models with adjacent deformation sources and have tested them against the solutions of corresponding 3-D finite element models, which account for the interaction between sources. We have tested various double-source configurations with either two spherical sources representing magma chambers, or a magma chamber and an adjacent dyke, modelled by a rectangular tensile dislocation or pressurized crack. For a tensile Okada source (representing an opening dyke) aligned or superposed to a Mogi source (magma chamber), we find the discrepancies with the numerical models to be insignificant (<5 per cent) independently of the source separation. However, if a Mogi source is placed side by side to an Okada source (in the strike-perpendicular direction), we find the discrepancies to become significant for a source separation less than four times the radius of the magma chamber. For horizontally or vertically aligned pressurized sources, the discrepancies are up to 20 per cent, which translates into surprisingly large errors when inverting deformation data for source parameters such as depth and volume change. Beyond 8 radii however, we demonstrate that the summation of analytical sources represents adjacent magma chambers correctly.

Key words: Numerical approximations and analysis; Mechanics, theory, and modelling; Physics of magma and magma bodies; Volcano monitoring.

1 INTRODUCTION

Analytical models of volcano deformation are available for sources of various simple geometries generally embedded in a homogeneous, isotropic and elastic half-space. Magma chambers and magmatic conduits are either modelled as a pressurized point source (Mogi 1958; Okada 1992) or as finite sources of various shapes, such as a sphere (McTigue 1987), a vertically elongated ellipsoid (Bonaccorso & Davis 1999), or a horizontal penny-shaped or elliptical crack (Fialko *et al.* 2001). Dykes are modelled as vertical or inclined finite elliptical pressurized cracks (Pollard & Holzhausen 1979; Davis 1983) or as finite rectangular dislocation sources opening evenly (Okada 1985, 1992). Although pressurized models are more realistic, Davis (1983) demonstrated that the discrepancies are negligible between the vertical surface displacements computed for a pressurized elliptical crack and for a rectangular dislocation source of identical volume. Some models account for viscoelastic crustal behaviour (Dragoni & Magnanensi 1989; Piombo *et al.*

2007), nevertheless the following study will be restricted to purely elastic behaviour as imposed in the Mogi point source and Okada rectangular dislocation source, hereafter referred to as 'Mogi' and 'Okada' models.

The Mogi and Okada models are certainly the most widely used analytical models to calculate surface deformation related to the pressurization of a magma chamber or the opening of a dyke (e.g. Sturkell 2003; Abidin *et al.* 2005; Sanderson *et al.* 2010; Stiros *et al.* 2010; Hughes 2011). This is due to the fact that they explain well many deformation patterns through simple equations governed by only a few parameters (Dvorak & Dzurisin 1997; Masterlark 2007). These two analytical models simplify the geometry and physical properties of the magmatic system and its surrounding. The elasticity assumption implies that displacements on the source walls must be infinitely small compared to the source main dimensions. The deformation source is embedded in a homogeneous and isotropic elastic half-space, the half-space assumption implying a flat and stress-free surface. For the source walls to be stress free, outside of the pressurization or opening, the Mogi point source must be located at a depth more than five times its radius (Lisowski 2007). In this simplified approach, several aspects are neglected: the properties of the magma within the source, such as its compressibility (Rivalta & Segall 2008), the surface topography, and the 3-D heterogeneities in the crust.

Several studies comparing numerical and analytical results have quantified the errors introduced when these aspects are neglected. Neglecting the topography or variations in the mechanical properties of the crust can introduce significant errors when predicting the surface deformation and when estimating the volume change of the source or its depth (e.g. Cayol & Cornet 1998; Williams & Wadge 1998; Lungarini *et al.* 2005; Masterlark 2007; Long & Grosfils 2009; de Zeeuw-van Dalfsen *et al.* 2012).

Magmatic systems are often represented by a combination of several sources if a single source model does not explain a complex data set. Many systems are modelled with a magma chamber where the magma originates and propagates either towards the surface or laterally through a dyke/conduit. Examples for this set of models are Mt Etna, Sicily (Palano *et al.* 2008, *cf.* Model C), Stromboli Volcano, Aeolian Islands (Bonaccorso *et al.* 2008), Kilauea Volcano, Hawaii (Yang & Davis 1992) and Izu islands, Japan Nishimura *et al.* (2001). Occasionally, magma chambers are also placed side by side to a dyke, for example at Krafla Volcano, Iceland (Arnadóttir *et al.* 1998), or at Kilauea Volcano, Hawaii (Montgomery-Brown *et al.* 2010). When the magmatic system is modelled with several magma chambers, those are either vertically stacked or more often stacked with a horizontal offset, for example at Unzen Volcano, Japan (Kohno *et al.* 2008), Long Valley Caldera, California (Tiampo *et al.* 2000). In these various cases, different analytical deformation sources are combined, and their respective deformation fields are summed. However, by doing so, the homogeneous half-space assumption is violated, in the sense that the source interaction is neglected. This interaction has been addressed in engineering studies in 2-D and 3-D for cracks, holes or cavities subjected to a far-field tension or compression (Gdoutos 1981; Kachanov 1987, 2003; Grechka & Kachanov 2006; Gorbatikh *et al.* 2007). However these studies have focused on the estimation of the effective crustal elasticity or stress intensity factors. For 2-D cavities, Jaeger *et al.* (2007, p. 250) pointed out that if the cavity is not located too close to any adjacent cavities or other boundaries, such as the ground surface, the infinite rock mass assumption (homogeneous half-space) is reasonable. Accordingly, the nearest distance to another cavity or other type of boundary should be at least three times the characteristic dimension of the cavity in order for this assumption to be met. However, the effect of source interactions in the context of volcano surface deformation, and for various arrangements of Mogi and Okada sources (i.e. in 3-D), has not been addressed yet. Such interaction introduces uncertainties additional to those caused by neglecting topography and heterogeneities. In this study, it is our aim to isolate and quantify these uncertainties. We investigate the discrepancies induced when combining several Mogi and Okada sources by testing the combined analytical solutions against the comprehensive numerical solutions. We determine the limitations of summing analytical Mogi and Okada solutions and quantify the errors induced.

2 METHOD

A common benchmark test in deformation modelling is the comparison between analytical and numerical solutions of equivalent models. The analytical models simplify the physical problems and solve the equations of elasticity, while satisfying a set of assumptions at any point of a volume. Finite elements (FE) models solve the complete set of elasticity equations at certain locations only (e.g. at mesh nodes) of a finite volume, satisfying the physical constraints given by the boundary conditions. The displacement within elements is then interpolated from the nodal displacements. On the one hand, comparing a simple numerical solution with its corresponding analytical solution allows us to calibrate the numerical models. On the other hand, when several Mogi and Okada sources are combined, we can evaluate the discrepancies between the sum of the analytical solutions and their corresponding numerical model solutions. We used COMSOL Multiphysics® as a FE modelling package and list the range of model parameters in Table 1 (see also the more detailed Table A-1 in the supporting information).

2.1 Numerical FE models equivalent to the Mogi and Okada models

Several issues have to be addressed before an FE model equivalent to Mogi and Okada models could be found. First, the homogeneous half-space assumption of the Mogi and Okada models is reproduced in the FE models by a large enough elastic volume and by zero-displacement conditions on its lateral and bottom boundaries. The domain is chosen big enough for these boundary conditions not to distort the numerical solution. The surface, that is the top boundary of the volume, is flat and stress free.

Secondly, the compromise between the computational capacity and the resolution of the mesh influences the accuracy of the solution and defines a discrepancy threshold of 5 per cent, that we consider significant.

Finally, although being a point source, the Mogi model is employed to compute the ground deformation due to spherical magma chambers. Hence we model it numerically as a pressurized spherical cavity embedded in the elastic domain, the source pressurization being applied as a vector normal to the cavity walls.

The Okada source can be numerically modelled using several approaches. In the three methods tested in this study (Fig. 1), the deformation source is composed of two rectangular surfaces representing the dyke walls, initially welded. An 'identity pair' condition is imposed on the two surfaces surrounding the dyke, to ensure the continuity of the deformation field in the elastic medium. The boundary conditions applied on the dyke walls depend on the

Table 1. Geometry and physical parameters for Models A–D (* tested with Model A–G1 only). In all models, a Poisson's ratio of $\nu = 0.25$ and a Young's modulus of $E = 10$ GPa are used. The dyke, of width and length 1 km, is modelled in the FEM with Methods 1–3 described in text. Note: Model 'A-G2d' refers to superposed sources ('A'), source with radius of 50 m and the upper source radius-to-depth ratio of 0.05 ('G2'), and a source separation of 5 radii ('d'). Model 'DI-M2a' refers to a spherical source juxtaposed to a dyke ('DI') at a distance of 1.5 radii ('a'), the dyke being modelled numerically with Method 2 (one of the dyke walls is displaced relative to the other). See also Table A-1 in supporting information for more details on numerical models and their benchmarking.

Model	Group	Source radius a (m)	a/d ratio	Source separation (a–f) (radii)	Source 1 $\Delta P1$ (MPa)	Source 2 $\Delta P2$ or opening U_{op}
A	G1a–f	50	0.1	2.5, 3, 4, 5, 8, 10	Upper source	Lower source
	G1'a–f	500	0.1	2.5, 3, 4, 5, 8, 10	20	20 MPa
	G2a–f	50	0.05	2.5, 3, 4, 5, 8, 10	20	−20 MPa
	G3a–f	500	0.5	2.5, 3, 4, 5, 8, 10	200*	200* MPa
B	G1a–f	50	0.1	2.5, 3, 4, 5, 8, 10	Upper source	Right-hand s.
	G1'a–f	500	0.1	2.5, 3, 4, 5, 8, 10	20	20 MPa
	G2a–f	50	0.05	2.5, 3, 4, 5, 8, 10	20	−20 MPa
	G3a–f	500	0.5	2.5, 3, 4, 5, 8, 10		
C	a–f	500	<0.2	1.5, 2, 3, 4, 7, 9	Lower source 20 MPa −20 MPa Right-hand s.	Upper source 1 m 1 m Left-hand s.
DI	M1a–f	500	0.2	1.5, 2, 3, 4, 7, 9	20 −20	1 m 1 m
	M2a–f	500	0.2	1.5, 2, 3, 4, 7, 9	20 −20	1 m 1 m
	M3a–f	500	0.2	1.5, 2, 3, 4, 7, 9	20 −20 Right-hand s.	12 MPa 12 MPa Left-hand s.
DII	a–f	500	0.2	1.5, 2, 3, 4, 7, 9	20 −20	1 m 1 m

method employed. In the first numerical approach ('Method 1'), we apply constant normal displacement of $\pm U_{op}/2$ to the wall of a vertical dyke (Currenti *et al.* 2008; Pulvirenti *et al.* 2009), such that U_{op} is the total opening of the dyke and the centre of the dyke is fixed in space. Note that, in contrast to our numerical Method 1, the central plane of an inclined or horizontal Okada source is not fixed, but is shifted towards the free surface. In the second approach ('Method 2'), we impose a constant displacement U_{op} between the two dyke walls without fixing their location. Methods 1 and 2 will provide identical results if no second source is employed. However, Method 2 can account for the response of the dyke geometry to the stress-field of a secondary source. Finally, Davis (1983) showed that the vertical displacements due to a rectangular tensile source and a pressurized elliptical crack after Pollard & Holzhausen (1979) are similar when their volume change is similar and their depth-to-top is deep enough, that is at a ratio of depth to half-length of 1.25. Hence in 'Method 3', although the dyke is not elliptical but tabular, we model it as a pressurized source with a volume change equivalent to the one of the analytical Okada source (Fig. 1).

2.2 Description of models scenarios A–D

The surface displacements induced by Mogi and Okada sources are controlled by the geometry, the volume change of the source(s), and by the elastic properties of the medium. In this study, we focus on the effect of the model geometry and show results from more than 150 models in which we vary:

(i) source geometry (spherical and/or rectangular sources)
(ii) source separation
(iii) relative source position
(iv) ratio between radius and depth of spherical sources
(v) pressure difference between spherical sources and medium.

Two main types of models are considered, with either two spherical sources (Models A and B) or one spherical and one rectangular source (Models C and D). Geometrically, the sources are arranged such that their centres are either lined-up vertically (Models A and C), horizontally in the strike-perpendicular direction (Models B and DI), and horizontally in the strike-parallel direction (Model DII). In the following, we will refer to these three geometries as models with 'superposed', 'juxtaposed' and 'aligned' sources, respectively. All models are schematized in Fig. 2 and their geometrical and physical parameters are listed in Table 1. For all models, the medium Poisson's ratio and Young's modulus were fixed to $\nu = 0.25$ and $E = 10$ GPa, respectively.

In Models A and B, the two sources, identical in size, are either superposed (Models A) or juxtaposed (Models B). The Mogi source radius (a) is set to 50 or 500 m. We vary the depth (d) of the upper source (source 1) such that its radius/depth ratio is either 0.1 (Groups G1 and G1', with a 50 and 500 m, respectively), 0.05 (Group G2) or 0.5 (Group G3). In the last case of $a/d = 0.5$, the source is too close to the surface (McTigue 1987), violating the point source assumption of the Mogi model, thus we have employed the finite source analytical solution given by McTigue (1987). Various pressure differences have been tested, for example in Model A $\Delta P_1 = \pm\Delta P_2 = 20$ MPa or $\Delta P_1 = \Delta P_2 = 200$ MPa, where ΔP_1 and ΔP_2 is the overpressure of the upper and the bottom sources, respectively.

In Models C and D (Fig. 2) the Mogi and Okada sources are either superposed (Model C), juxtaposed (Model DI), or aligned

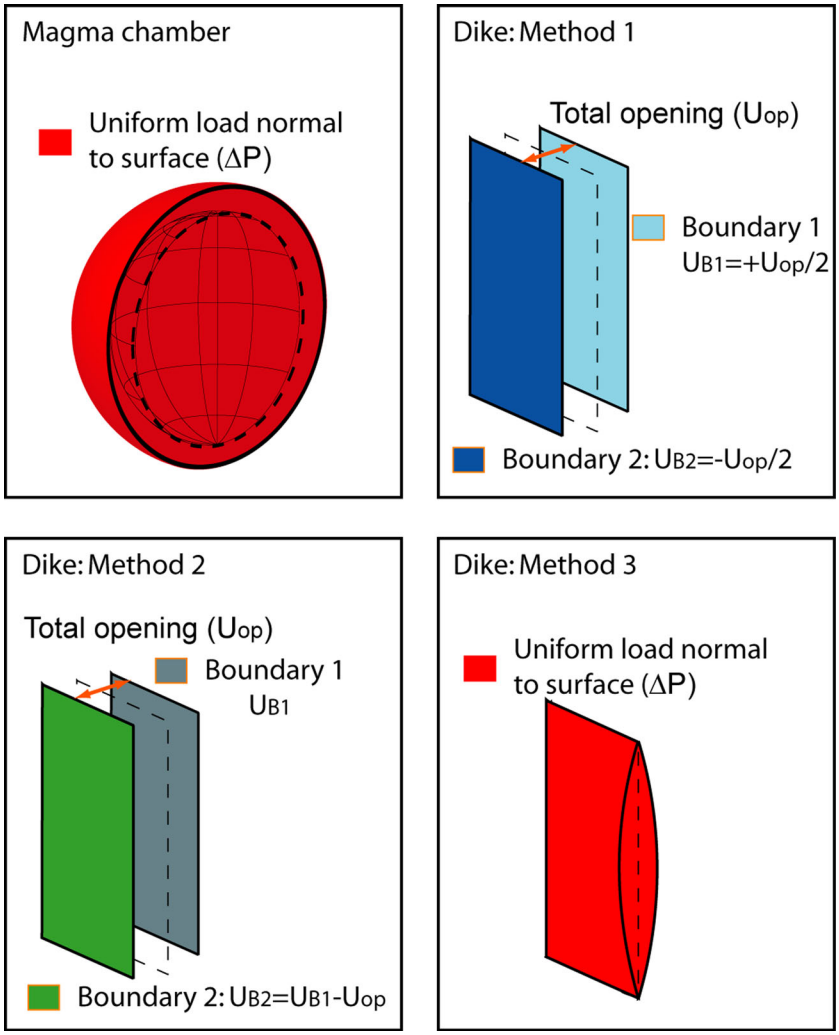

Figure 1. Finite element numerical methods employed to model a spherical pressurized source and a dyke source equivalent to the analytical Mogi and Okada sources. Magma chamber: a load is applied normal to the spherical source. The dyke is modelled with three different methods. Method 1: a constant normal displacement of $\pm U_{\rm op}/2$ is applied to the dyke walls; Method 2: a constant displacement $U_{\rm op}$ is applied between the two dyke walls without fixing their location; Method 3: a pressure normal to the dyke walls is applied such that its volume change corresponds to the volume of the analytical Okada source.

(Model DII). The dimensions of the Okada source are set to 1 × 1 km with an opening of 1 m and depth-to-top of 1 km (Model C), or 2 km (Models D). The Mogi source radius is set to 500 m, and the pressure difference $\Delta P = \pm 20$ MPa. The centre-to-centre distance separating the sources ranges from 2.5 to 10 times the source radius in Models A and B and the separation between the Mogi source centre and the closest boundary of the Okada source varies from 1.5 to 9 source radii in Models C and D.

2.3 Estimation of discrepancies

For all scenarios considered, we calibrate the numerical sources against the analytical sources independently before running the combined source models. In order to estimate the errors, we calculate the mean surface absolute discrepancies ϵ (eq. 1) following Currenti *et al.* (2008), and the local discrepancies Ξ (eq. 2) at the maximum ($U|_{\rm max}$) or the minimum ($U|_{\rm min}$) of the vertical or horizontal surface displacements. These two estimates have been chosen because ϵ relates to a datafit involving an entire data set, while Ξ links to the modelling process employing a single datapoint at the maximum.

The average of the absolute discrepancies ϵ [per cent] is computed at each surface node normalized by the average surface analytical solution $\overline{U^{\rm An}}$,

$$\epsilon_j = \frac{\sum_{i=1}^{N} \frac{\left|U_{ji}^{\rm An} - U_{ji}^{\rm FE}\right|}{N}}{\sum_{i=1}^{N} \frac{\left|U_{ji}^{\rm An}\right|}{N}} \times 100, \qquad (1)$$

with $U_{ji}^{\rm An}$ and $U_{ji}^{\rm FE}$ being the analytical or numerical horizontal (U_{xi}, U_{yi}) or vertical (U_{zi}) surface displacements (in m) calculated at the surface node i located at coordinates (x, y, 0) (in m), with N being the total number of surface nodes.

The local discrepancies (Ξ, in per cent) correspond to the normalized difference at the minimum ($\Xi_x|_{\rm min}$, $\Xi_z|_{\rm min}$) or maximum ($\Xi_x|_{\rm max}$, $\Xi_z|_{\rm max}$) of the analytical and numerical surface

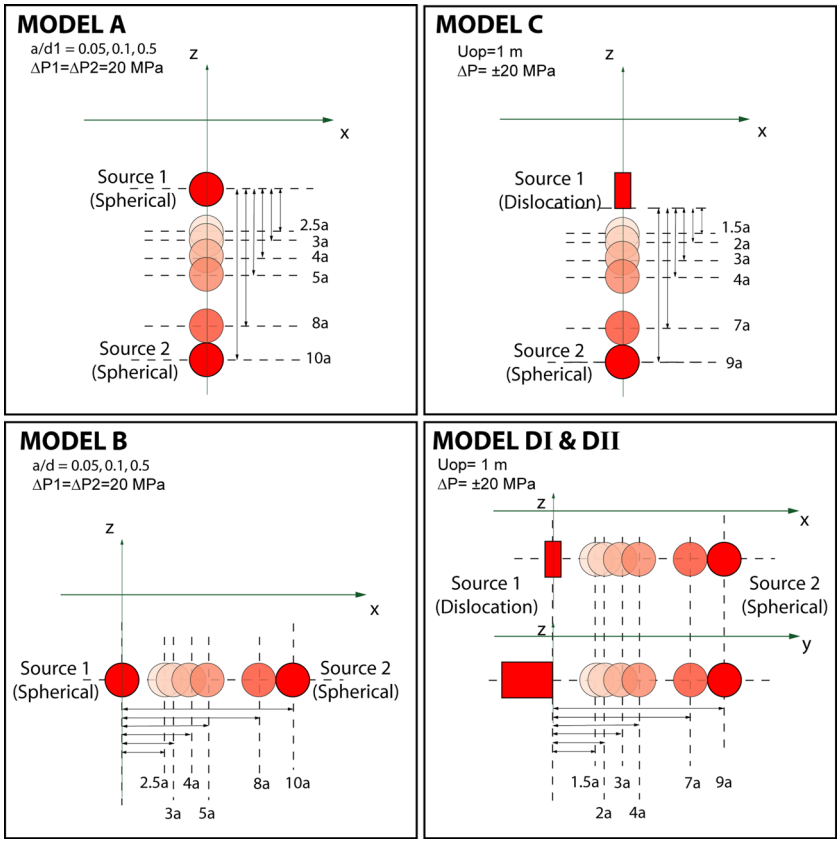

Figure 2. Model scenarios. Two spherical sources superposed (Model A) or juxtaposed (Model B), close to models of for example Soufrière Hills Volcano, Montserrat, or Long Valley Caldera, California; One spherical and one dyke sources superposed (Model C), similar to models of for example Mt Etna and Stromboli Volcano; or one spherical source offset to a dyke in strike-perpendicular and strike-parallel directions referred to in text as 'juxtaposed' and 'aligned', respectively (Models DI and DII), such as for example Kilauea Volcano, Hawaii and Izu islands, Japan. The separation between the sources is increased from 2.5 to 10 radii (Models A and B) or 1.5 to 9 source radius unit (Models C and D). Geometry and physical parameters are listed in Table 1.

displacements. Taking $\Xi_x|_{\min}$ and $\Xi_z|_{\max}$ as examples:

$$\Xi_x\Big|_{\min} = \frac{\text{abs}\left\{U_x^{\text{An}}\Big|_{\min} - U_x^{\text{FE}}\Big|_{\min}\right\}}{\text{abs}\left\{U_x^{\text{An}}\Big|_{\min}\right\}} \times 100$$

$$\text{or} \quad \Xi_z\Big|_{\max} = \frac{\text{abs}\left\{U_z^{\text{An}}\Big|_{\max} - U_z^{\text{FE}}\Big|_{\max}\right\}}{\text{abs}\left\{U_z^{\text{An}}\Big|_{\max}\right\}} \times 100. \qquad (2)$$

During the calibration process, we have determined that the appropriate domain size and mesh density for the various models induce numerical errors of less than 5 per cent (see supporting information, Table 8). Smaller errors were achieved for the Mogi source models, with Ξ and ϵ less than 3 per cent. The calibration of the dyke modelled as either a dislocation tensile source (Methods 1 and 2) or as a pressurized tabular crack (Method 3) confirms that the surface displacements solutions of the three methods are similar to the Okada analytical solutions despite the different dyke shapes for depth-to-top of 1 and 2 km, if no second source is present (Fig. 3 and in Table A-1, in the supporting information).

Throughout this study, we use the domain dimensions and mesh density that have yielded the maximum error of 5 per cent during the calibration of the individual sources to investigate the combined models discrepancies. Furthermore, we compared the sum of the analytical solution of models combining Mogi and Okada sources with the sum of the individual numerical solutions of each source and found that the discrepancies are also negligible ['M1+M2' and 'M+0 (DIa)' in Table A-1]. Accordingly, discrepancies larger than 5 per cent will be considered as significant and caused by the presence of a second deformation source and resulting source interaction.

3 RESULTS

In the following sections, we present the results for superposed or juxtaposed spherical sources (Models A and B, respectively) and for juxtaposed dyke and spherical source (Model DI) that give significant discrepancies between analytical and FEM surface displacements. In the main body of the paper, we present a subset of the results for Models A, B and DI, and list the full set of results in the supporting information. Models with a spherical source and a dyke either superposed or aligned (Model C and DII, respectively) always yield negligible discrepancies (Table 2) and are not further described. The tables and figures in the supporting information are numbered with the prefix 'A-' .

3.1 Effect of source types and relative position

3.1.1 Models A and B: superposed and juxtaposed spherical sources

Models A and B results highlight how the discrepancies between analytical and numerical models depend on both geometry and on the combination of inflating or deflating sources.

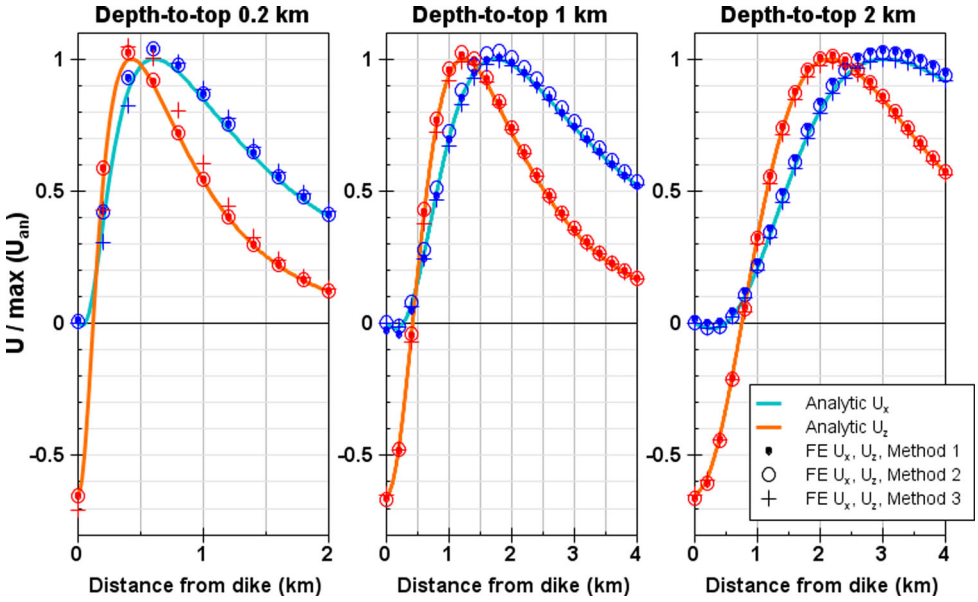

Figure 3. Surface displacements profiles for a dyke with depth-to-top at 0.2 km (left-hand panel), 1 km (centre panel) and 2 km (right-hand panel) calculated either analytically or computed using Methods 1–3. The dyke opens by 1 m and its height and width are 1 km. The horizontal U_x and vertical U_z surface displacements are normalized by $U_x^{\mathrm{An}}|_{\max}$ and $U_z^{\mathrm{An}}|_{\max}$, respectively. Note that in the absence of a secondary source and for a depth-to-top larger than 1 km all three methods yield similar results matching the analytical Okada solution.

Table 2. Models A–D: maximum discrepancies found either for various pressurization ($\Delta P1$, $\Delta P2$) of the two spherical sources in Models A–B or for various pressurization of the spherical source ($\Delta P1$) and various dyke opening (U_{op}, Methods 1–2) or dyke pressurization ($\Delta P2$, Method 3). D_{limit} [(1)] corresponds to the source separation where the discrepancies become negligible. In all models, the Poisson's ratio $\nu = 0.25$ and the Young's modulus $E = 10$ GPa.

Model #	$\Delta P1$ (MPa)	$\frac{\Delta P1}{\Delta P2}$	U_{op}	Maximum discrepancies obtained (per cent)					D_{limit} [(1)] (radii)
				ϵ_x	ϵ_y	ϵ_z	Ξ_x	Ξ_z	
A, G1a	20	1	n/a	3.3	3.3	5.6	7.0	13.9	4
	200	1	n/a	3.3	3.3	5.6	7.0	13.9	4
	10	1	n/a	3.3	3.3	5.6	7.0	13.9	–
	20	1/2	n/a	3.6	3.6	5.7	7.3	16.1	–
	40	2	n/a	3.1	3.1	5.5	6.6	12.0	–
	20	−1	n/a	6.5	5.6	11.4	7.2	13.6	4
	200	−1	n/a	6.5	5.6	11.4	7.2	13.6	–
	20	−1/2	n/a	8.5	8.5	7.6	1.5	16.2	4
B,G1'a	20	1	n/a	5.3	5.8	4.6	1.4	6.3	4
	200	1	n/a	5.3	5.8	4.6	1.4	6.3	–
	20	−1	n/a	9.6	13.1	12.3	8.9	13.8	4
Ca	20	n/a	1	1.3	1.2	1.6	1.2	1.5	<1.5
	−20	n/a	1	9.0	0.4	1.9	4.0	1.0	2
DI,m1	20	n/a	1 m	97.2	12.3	12.6	82.3	15.1	9+
	−20	n/a	1 m	553.7	9.8	22.5	298.8	5.3	9+
DI,m1	20	n/a	2 m	39.3	18.5	12.1	41.1	14.7	–
	−20	n/a	2 m	723.5	14.9	30.8	657.4	1.7	–
DI,m2	20	n/a	1 m	7.1	7.6	5.7	5.9	7.2	3
	−20	n/a	1 m	24.1	7.6	6.8	8.7	7.0	3
DI,m2	20	n/a	2 m	11.0	17.0	9.7	11.0	10.7	–
	−20	n/a	2 m	49.0	13.7	15.4	18.8	12.6	–
DI,m3	20	n/a	12 MPa	14.3	12.3	9.1	11.2	5.5	3
	−20	n/a	12 MPa	11.1	15.5	11.9	17.6	12.9	3
DI,m3	20	n/a	23 MPa	16.5	23.5	13.2	26.6	11.8	–
	−20	n/a	23 MPa	30.3	19.2	17.5	23.1	19.2	–
DII,m1	20	n/a	1	0.3	0.7	1.5	0.2	0.7	<1.5
	−20	n/a	1	0.9	1.4	1.4	0.7	1.7	<1.5

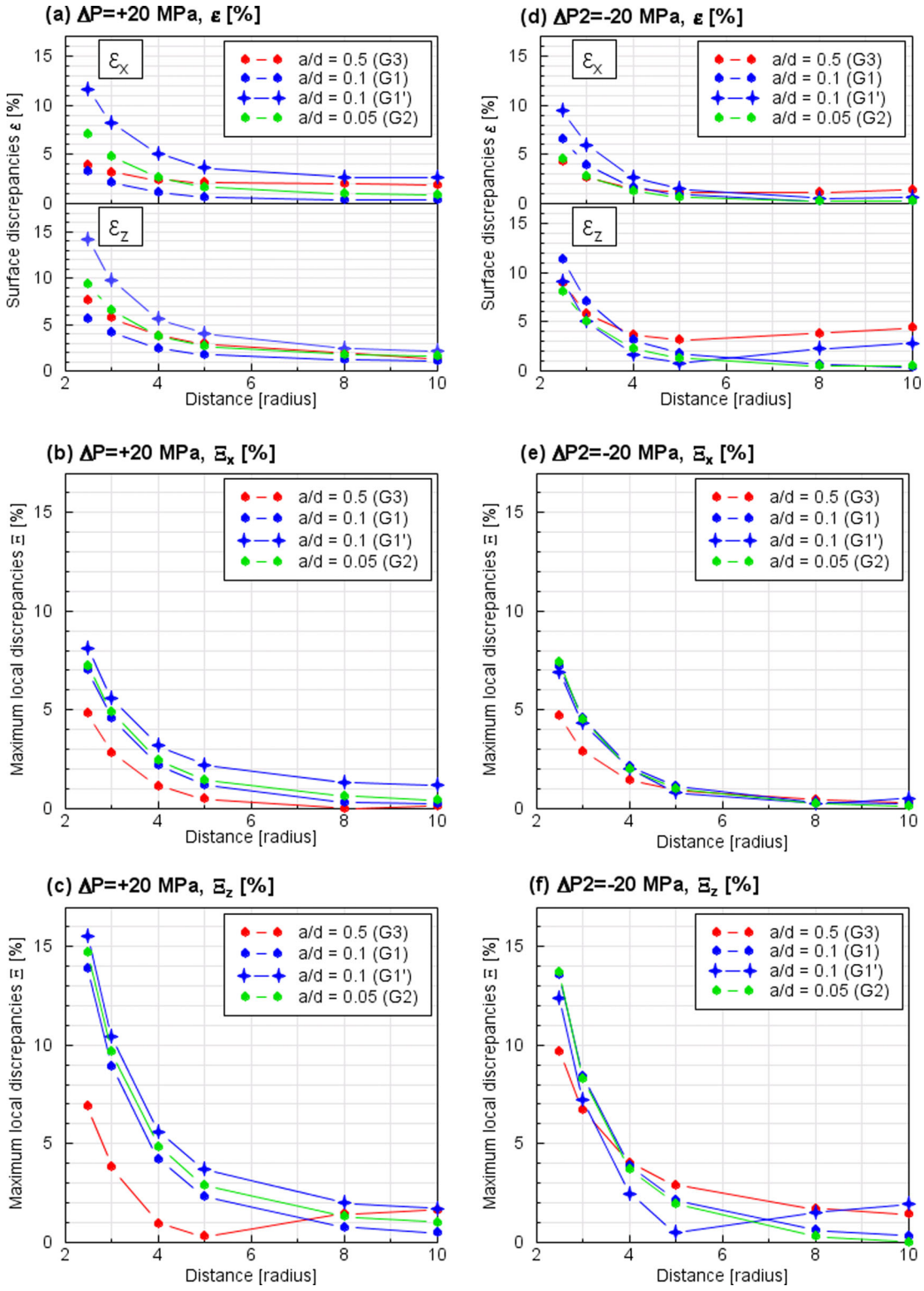

Figure 4. Model A: surface (ϵ) and maximum local (Ξ) discrepancies vs source separation, obtained for models combining two superposed spherical sources. The shallower source is pressurized by $\Delta P_1 = +20$ MPa and the deeper source is either pressurized by $\Delta P_2 = +20$ MPa (left-hand column: a–c) or underpressurized by $\Delta P_2 = -20$ MPa (right-hand column: d–f). Corresponding discrepancies values are listed in Table A-2.

When the two sources are inflating, superposed sources (Model A) produce overall greater discrepancies than juxtaposed sources (Model B): for example for Model A, at 2.5 radii separation, ϵ, Ξ_x and Ξ_z are 14, 8 and 16 per cent, respectively, while for Model B ϵ reaches 7 per cent, Ξ_x is always negligible and Ξ_z is 10 per cent (Figs 4 and 5, Tables A-2 and A-3). However, when one of the sources is deflating, the discrepancies for both models are similar. For Models A and B, all discrepancies are negligible (<5 per cent) beyond a source separation (centre-to-centre) of 4 radii.

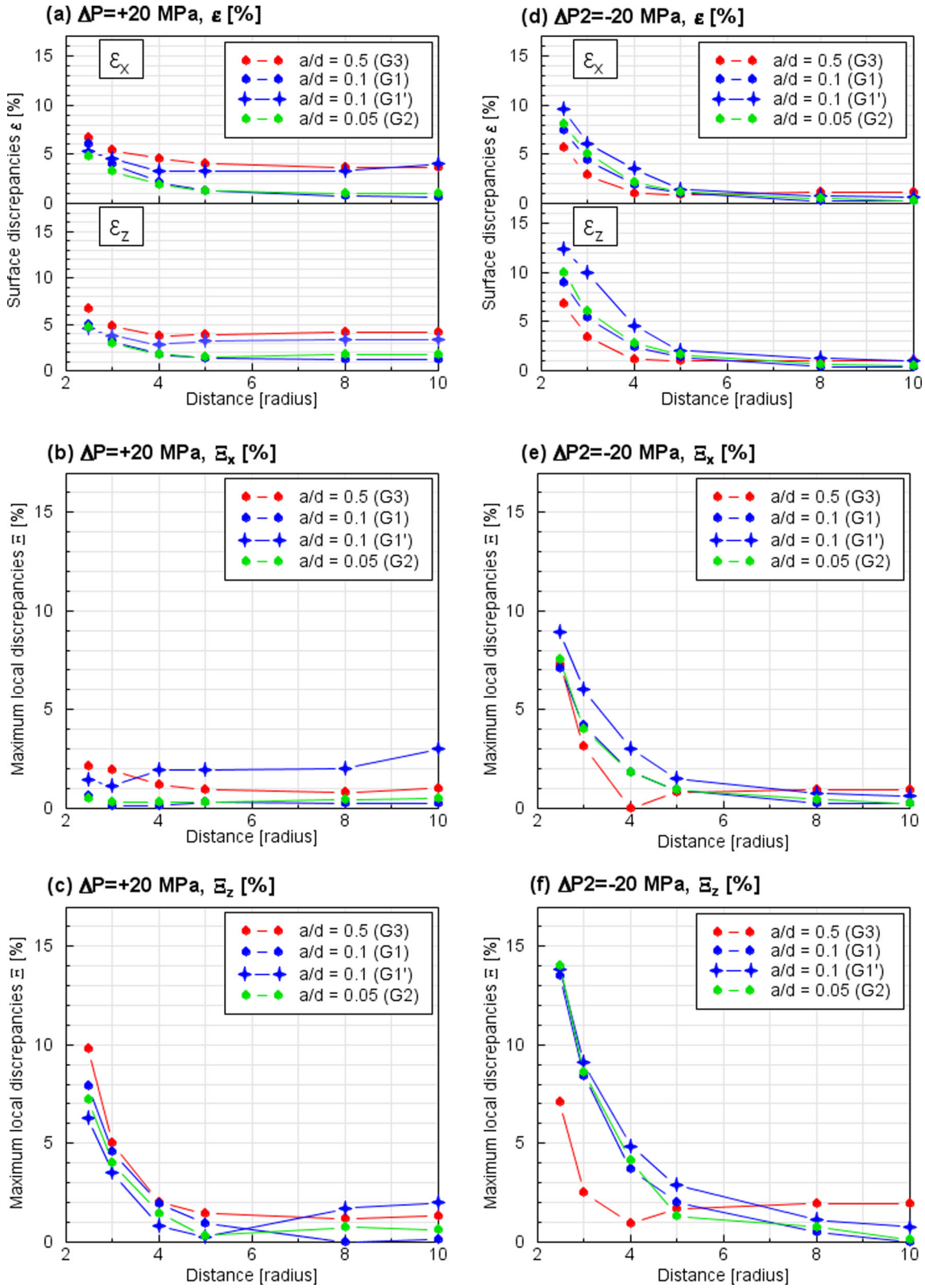

Figure 5. Model B: surface (ϵ) and maximum local (Ξ) discrepancies vs source separation, obtained for models combining two juxtaposed spherical sources, one of them being pressurized by $\Delta P_1 = +20$ MPa and the other one being either pressurized by $\Delta P_2 = +20$ MPa (left-hand column: a–c) or pressurized by $\Delta P_2 = -20$ MPa (right-hand column: d–f). Corresponding discrepancies values are listed in Table A-3.

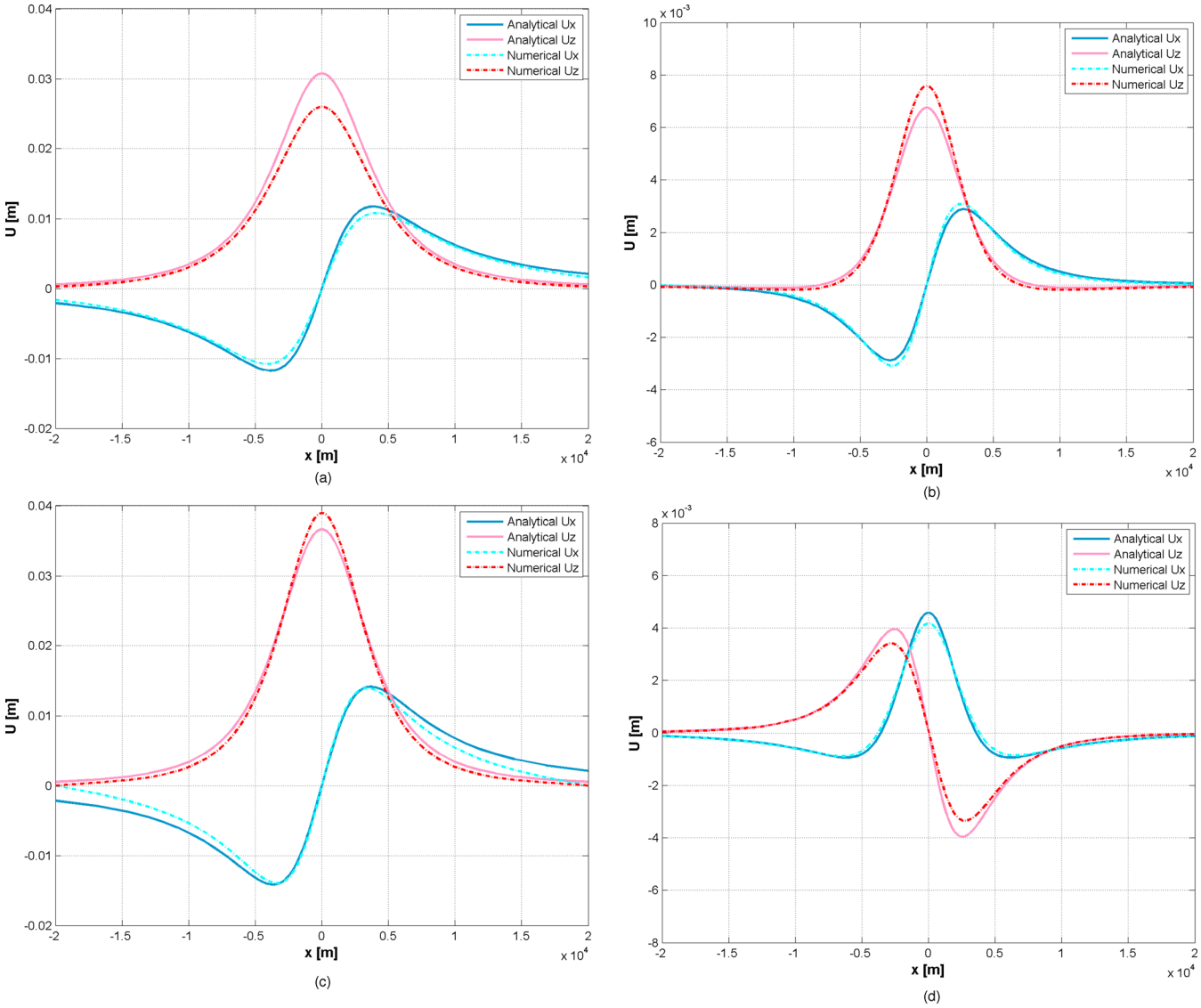

Figure 6. Models A and B (Group G1'a): surface displacements across the centre of the deformation sources for models with two superposed (Model A) or two juxtaposed sources (Model B) separated by a distance of 2.5 radii. The lower of right-hand source (Source 2) pressurization is either $\Delta P2 = 20$ MPa (left-hand column: a, c) or $\Delta P2 = -20$ MPa (right-hand column: b, d). The profiles for further source separation are presented in Figs A-2 and A-3.

Depending on the position of the sources and their pressurization (inflation or deflation) the analytical models either under- or overestimate the surface displacements (Fig. 6). Two overpressurized sources 'shield' each other and their inflation is buffered where the sources are the closest (Fig. 7a). However, when one of the two sources is inflating and the second deflating, the former expands into the space vacated by the latter, this effect being the strongest where the sources are the closest (Fig. 7b). At the surface, for both Models A and B, the discrepancies are significative (5 per cent) up to a horizontal distance of 3 km (U_x) and 5 km (U_z). In the case where two sources are superposed, the analytical solution overestimates both horizontal and vertical displacements for two inflating sources (Fig. 6a), but underestimates them for one inflating and one deflating source (Fig. 6b). In the scenario of two juxtaposed sources (Model B), the analytical model underestimates the surface displacements when the two sources are inflating or overestimates them when one of the sources is deflating (Figs 6c and d).

Finally, the discrepancies computed between the numerical solution and McTigue's finite spherical source solution (Group 3 in Models A and B) do not clearly differ from those calculated using Mogi's point source (Groups 1–2). The surface discrepancies ϵ are similar for Models A and B. In contrast, when the two spheres are superposed and inflating (Model A), the finite source solution reduces Ξ_x to 5 per cent (Groups 1–2: 8 per cent) and Ξ_z to 7 per cent (Groups 1–2: 15 per cent). In case of the juxtaposed sources (Model B), when one of the source is deflating, Ξ_x is similar but McTigue's solution reduces Ξ_z to 7 per cent (Groups 1–2: 14 per cent).

3.1.2 Model DI, Methods 1–3: juxtaposed tensile rectangular and spherical sources

The discrepancies computed for Model DI strongly depend on the approach employed to model the opening dyke (Fig. 1). The results of the three approaches (Methods 1–3) are compared in Fig. 8, in Fig. A1, and in Fig. 9 (see also Table A-5). The conditions applied on the dyke boundaries (displacements or pressure) are directly related to the way the sources can deform and influence each other (Fig. 10).

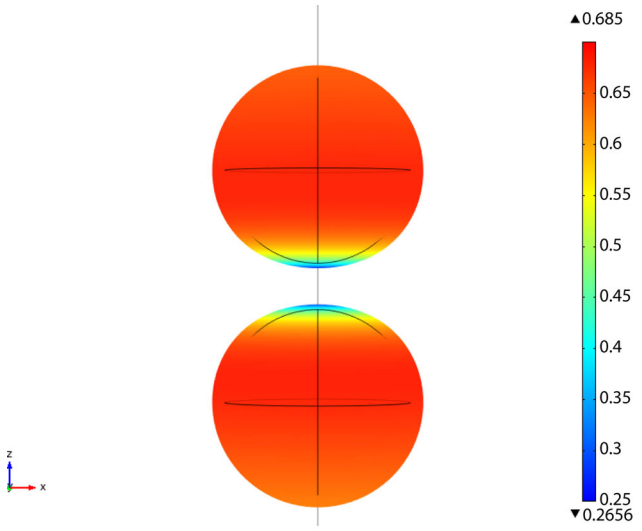

(a) Model A ($\Delta P1 = \Delta P2 = 20$ MPa)

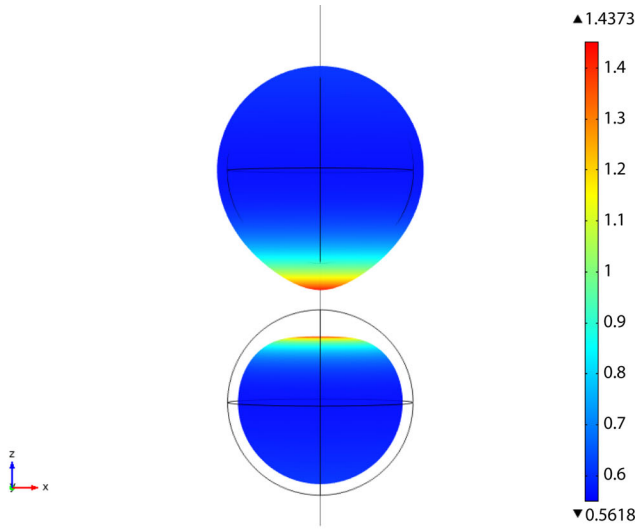

(b) Model A ($\Delta P1 = -\Delta P2 = 20$ MPa)

Figure 7. Models A (Group G1'a): Cross-section of the source total deformation (m) of a spherical source pressurized by $\Delta P1 = 20$ MPa superposed to another spherical source pressurized by either $\Delta P2 = 20$ MPa (left-hand panel) or $\Delta P2 = -20$ MPa) (right-hand panel), in an homogeneous medium. The source deformation is magnified by a factor of 100.

Using Method 1, a fixed displacement prescribed on both dyke walls immobilizes the dyke, prevents its deformation, and only the spherical source deforms. Method 1 gives analytical and numerical surface displacements that differ radically in the dyke opening direction (the x direction for the models considered). Consequently, the discrepancies (ϵ and Ξ) in this direction are two orders of magnitude larger than in the other directions (see Table A-4). When the spherical source inflates, ϵ_x and Ξ_x reach 97 and 82 per cent (Fig. A1). They even reach 550 and 300 per cent, respectively, when the spherical source deflates (Fig. 8). The remaining discrepancies in vertical (ϵ_z) and strike (ϵ_y) directions are, however, of the same order of magnitude as those computed for Models A and B: ϵ_z and Ξ_z are up to 13 and 15 per cent for an inflating sphere and up to 23 and 5 per cent for a deflating source. All discrepancies become negligible beyond 9 radii separation.

In contrast to Method 1, when using Methods 2 and 3 (displacement of a flexible dyke wall with constant opening, or pressurized tabular crack) all discrepancies are of comparable magnitude to models A and B. With these two methods (2 and 3), both the dyke and the spherical source can deform (Fig. 10). This is reflected in the magnitude of the surface discrepancies: while ϵ_y is on average lower than both ϵ_x and ϵ_z for a rigid dyke (Method 1), all components of the surface discrepancies are within 2 per cent for source separation of 3 radii and beyond. For both methods, neglecting the source interaction leads to significant discrepancies up to a horizontal distance of 5 km (U_x) and 3 km (U_z), with an underestimation of U_z and overall a slight overestimation of U_x (Fig. 9).

With Method 2, the dyke is simply 'pushed' away from or 'pulled' towards the inflating or deflating sphere, which in turn deforms in response to the dyke opening, constant over the dyke plane.

The discrepancies computed with Method 2, which is the closest to an Okada rectangular tensile dislocation, are on average the lowest calculated between the three methods, and are significant only up to 2 radii source separation (Fig. 8, and also Fig. A-1). Regarding the surface discrepancies, ϵ_x is still larger than ϵ_z, with 7 per cent versus 6 per cent and 24 per cent versus 7 per cent for inflating and deflating sphere, respectively. However Ξ_x and Ξ_z are similar, with maximum values for Ξ_x and Ξ_z of 6 and 7 per cent, respectively, for an inflating sphere, and 9 and 7 per cent for a deflating source.

A pressurized tabular crack, Method 3, does not open uniformly as the Okada analytical model or Methods 1 or 2, but deformation of the dyke walls results in a bulging shape (Fig. 1). In the presence of an additional inflating or deflating source, the resulting shape will be more complex (Fig. 10). The discrepancies are overall intermediate to those calculated with the two other methods and become negligible beyond 3 radii separation (Fig. 8). This is the most realistic model for a pressurized dyke.

3.2 Effect of the radius/depth ratio

In Models A and B, the effect of the distance between sources and free surface has also been tested with various (upper source) radius/depth ratios (a/d) and was found to generally have little influence on the magnitude of the discrepancies: the surface discrepancies computed for $a/d = 0.1$ and 0.05 are all within 5 per cent, and Ξ_x and Ξ_z differ less than 2 per cent. Models with superposed inflating sources separated by 2.5 radii are an exception, with ϵ computed for a $a/d = 0.1$ with $a = 500$ m being 10 per cent larger than for the same ratio but with $a = 50$ m (Model A-Group G1a and G1'a, Fig. 4). Overall, independent of the a/d ratio, the discrepancies always follow the same trend and are all negligible beyond 4 radii separation.

3.3 Effect of source strength and geometry (Models A + Models DI)

The results listed in Table 2 underline the fact that the discrepancies vary with the pressure difference or displacements applied to the spherical or dislocation source walls. For the three models A, B and DI, we found that the discrepancies are in general larger if one of the sources is deflating.

Table 2 also highlights how far the discrepancies depend on the geometry. Discrepancies are higher for Model DI than for Models A and B, although they decrease more rapidly and are only significant (>5 per cent) for source separation of less than 3 radii (Methods 2 and 3), and 4 radii for Model A.

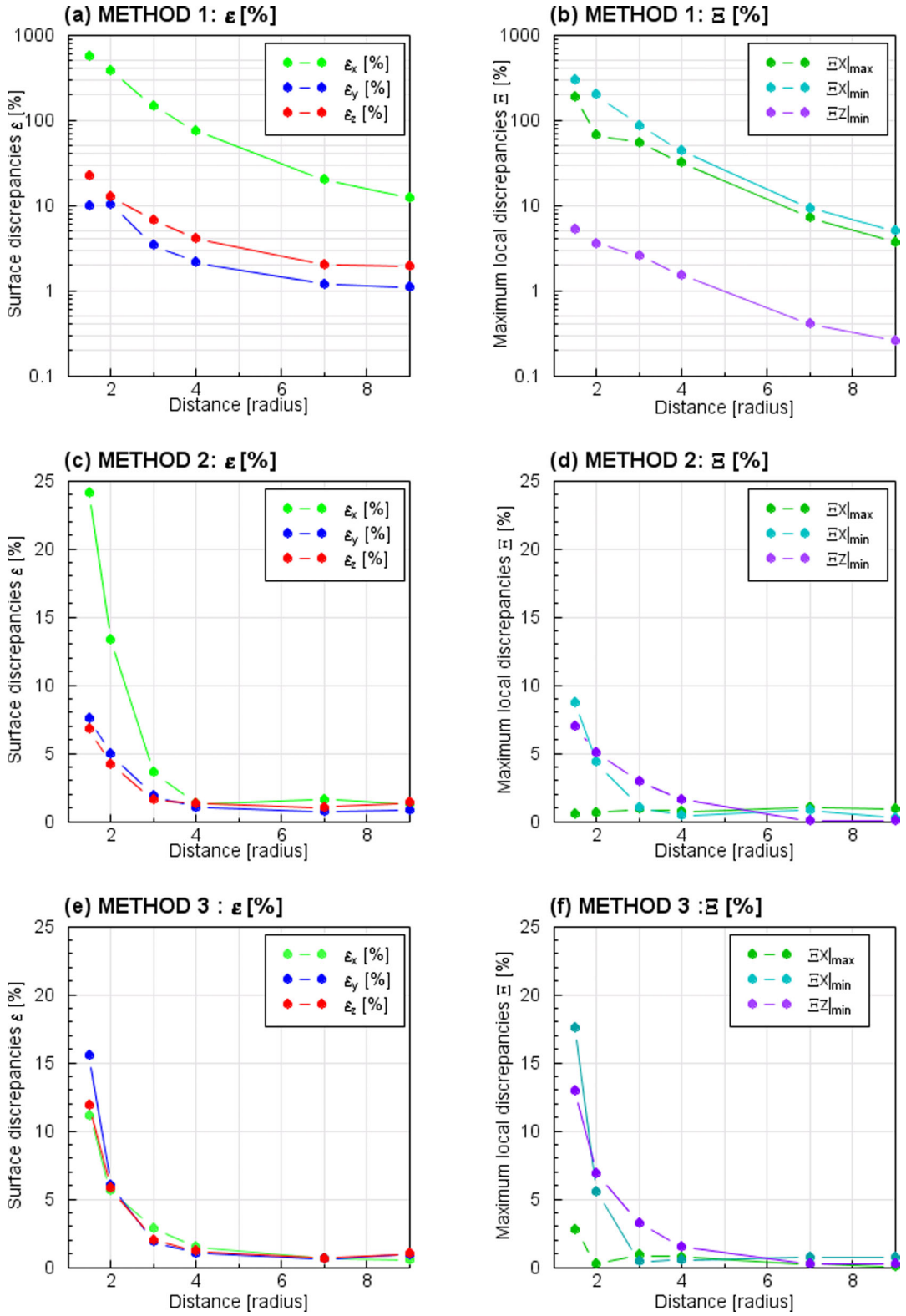

Figure 8. Model DI: surface (ϵ) and maximum local (Ξ) discrepancies vs source separation, obtained for models combining a spherical source pressurized by $\Delta P = -20$ MPa juxtaposed to a dyke opening by 1 m, modelled with Methods 1–3 (from top to bottom). Corresponding discrepancies values are listed in Table A-5.

The various pressure differences tested in Model A indicate that the discrepancies are identical for all multiples of the chosen $\Delta P1/\Delta P2$ ratio. The magnitude of discrepancies increases with the magnitude of the deeper source pressurization ($\Delta P2$) for a constant pressurization of the upper source ($\Delta P1$).

The various openings or pressures applied on the dyke wall in Model DI (Methods 2 and 3) also show that the closest results to the

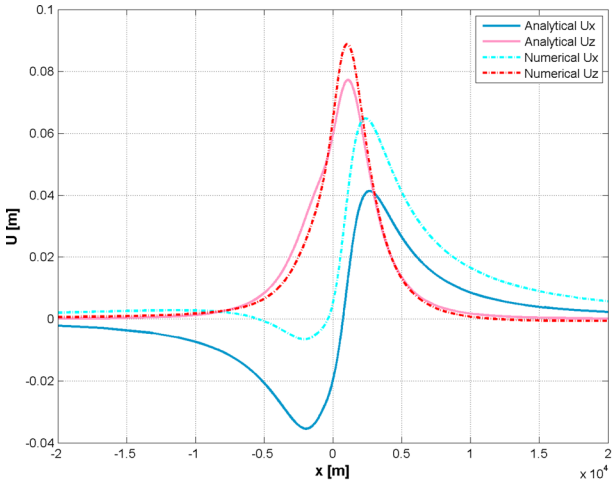

(a) Method 1, Distance 1.5 radii, $\Delta P = +20$ MPa

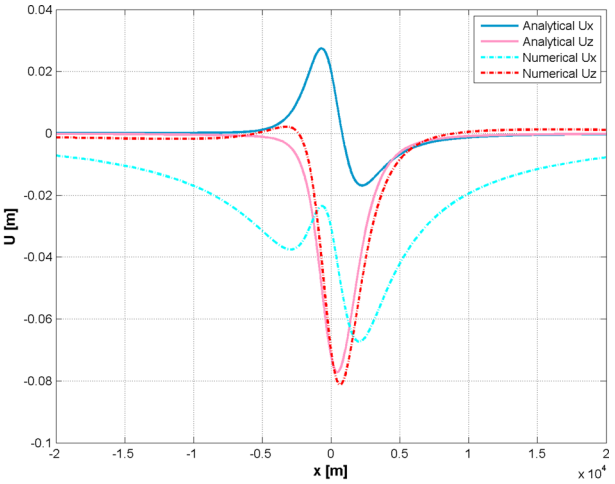

(b) Method 1, Distance 1.5 radii, $\Delta P = -20$ MPa

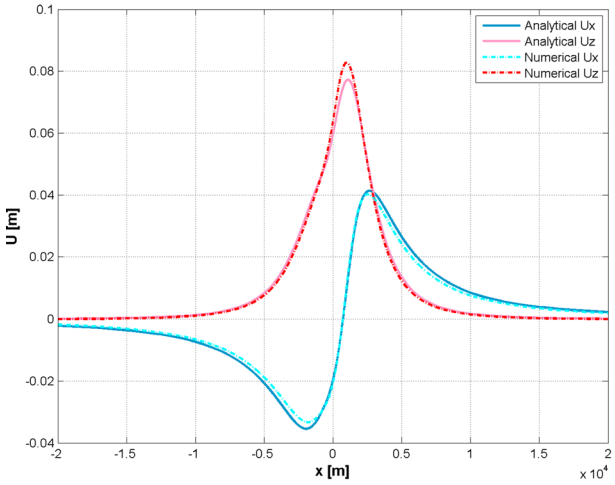

(c) Method 2, Distance 1.5 radii, $\Delta P = +20$ MPa

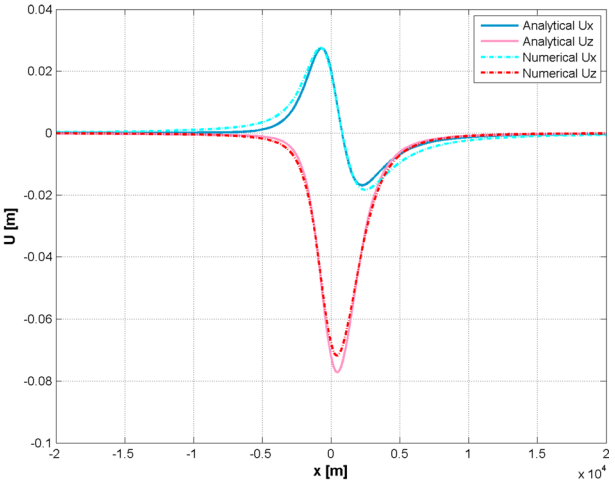

(d) Method 2, Distance 1.5 radii, $\Delta P = -20$ MPa

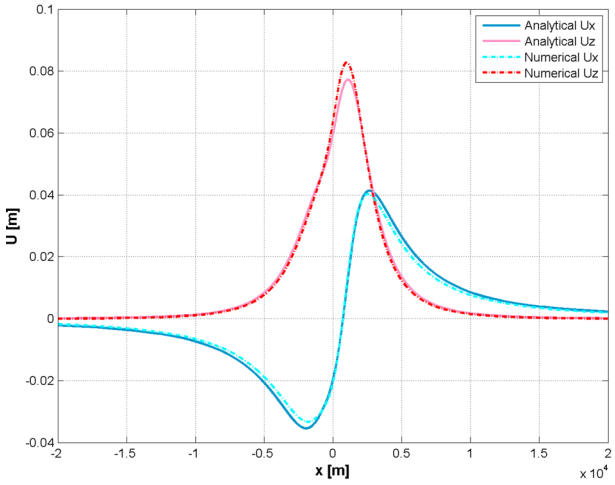

(e) Method 3, Distance 1.5 radii, $\Delta P = +20$ MPa

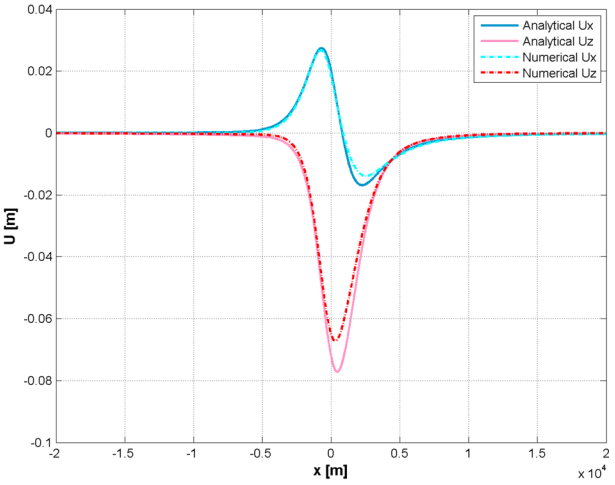

(f) Method 3, Distance 1.5 radii, $\Delta P = -20$ MPa

Figure 9. Model DIa: surface displacements across the centre of the deformation sources for models of a dyke opening by 1 m, modelled by Methods 1-3, juxtaposed to a spherical source pressurized by either $\Delta P2 = +20$ MPa (left-hand column: a, c and e) or $\Delta P2 = -20$ MPa (right-hand column: b, d and f). The sources are separated by a distance of 1.5 radii. The profiles for further source separation are presented in Figs A-4–A-6.

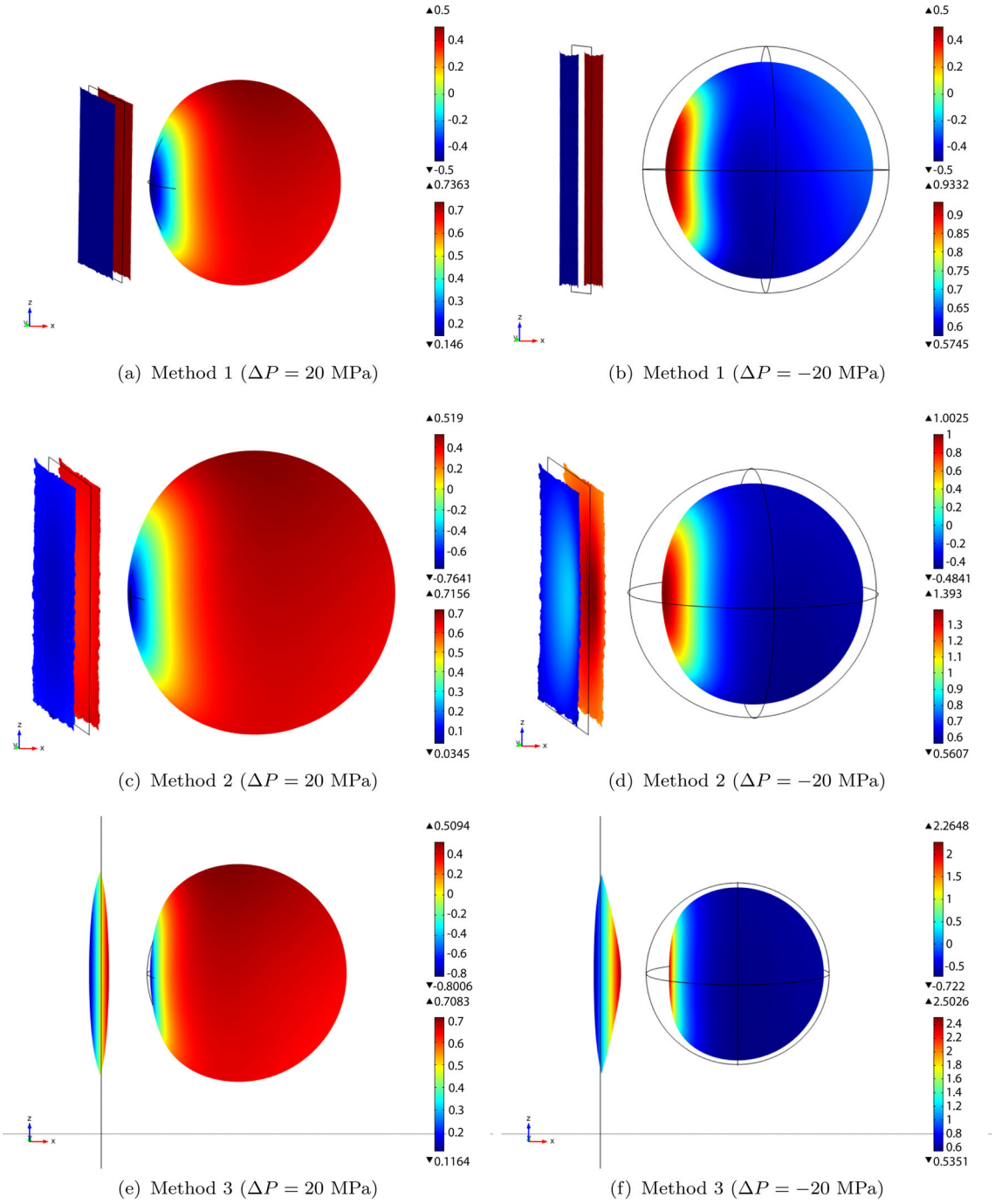

Figure 10. Models DI: cross-section of the source deformation (m) of a dyke opening by 1 m, modelled with Methods 1–3, juxtaposed to an inflating, $\Delta P = +20$ MPa (left-hand panel), or a deflating, $\Delta P = -20$ MPa, spherical source (right-hand panel), in an homogeneous medium. The distance between sources is 1.5 radii (Group DIa). The upper scale corresponds to the horizontal displacement of the dyke walls, to emphasize how Methods 1–3 differ. The lower scale corresponds to the total deformation of the spherical source. The source deformation is magnified by a factor of 100. Note that, with Method 1 (upper panel: a, b), only the spherical source is deforming.

analytical solution are generally given when the dyke is modelled with Method 2, with the exception of the surface discrepancies ϵ_x, which are closer to the analytical solution when modelled with Method 3.

3.4 Case studies

In the following section, we apply our methodology to three examples (referred as Models CS1-3) where analytical models were combined. In line with Section 2.2, we construct FE models with geometries and physical parameters equivalent to the analytical models presented in these case studies, which are depicted in Fig. 11, and their parameters are summarized in Table 3. We then calculate the discrepancies between FE and analytical models to estimate the effect of neglecting the source interactions.

We adapted these cases from Elsworth *et al.* (2008) and Linde *et al.* (2010) who employed analytical models to represent the volcanic plumbing system of Soufrière Hill volcano, Montserrat,

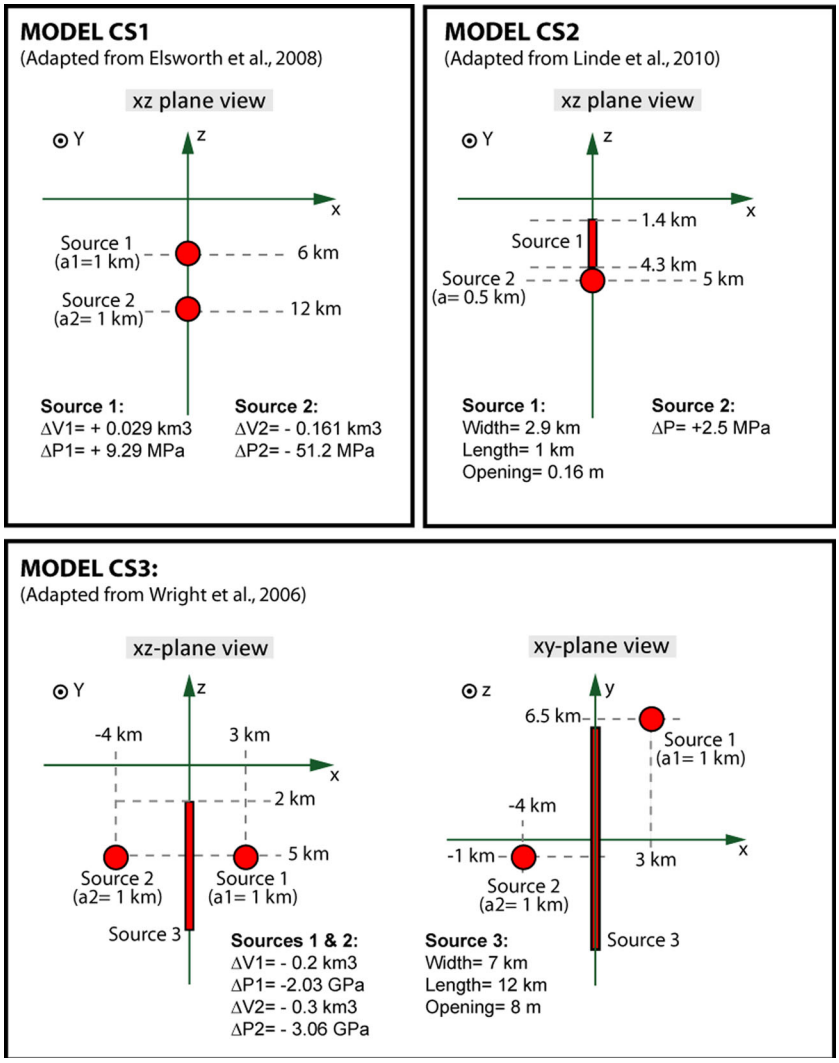

Figure 11. Case studies CS1-3. CS1 and CS2, corresponding to our Models A and C, respectively, are adapted from Elsworth *et al.* (2008) and Linde *et al.* (2010) analytical models of the plumbing system of Soufrière Hills Volcano, Montserrat, West Indies. CS3, corresponding to our Model DI, is adapted from the Dabbahu segment, Afar, Ethiopia magmatic system as described in Wright *et al.* (2006). Geometry and physical paarameters are listed in Table 3.

West Indies, for the first episode of unrest (1995 November 15–1998 March 10) and an explosion during 2004 March, respectively. The third case study Wright *et al.* (2006) modelled the magmatic system of the Dabbahu segment, Afar, Ethiopia, for the rifting episode that occurred between 2005 September 14 and October 4.

Model CS1, representing Soufrière Hills Volcano (SHV), consists of two superposed spherical magma chambers, and corresponds to our Model A with two superposed Mogi sources, separated by 6 source radii and with a ratio of source radius to depth of 0.17 (upper source). In Model CS2, the SHV magmatic system composed of a dyke (Okada source) superposed to a spherical pressure source (Mogi source).This model correspond to our Model C, with a distance between sources of 1.4 times the magma chamber radius. In Model CS3, we focus on the northern section of the Dabbahu-Gab'ho segment (Wright *et al.* 2006; Ayele *et al.* 2009), where two deflating magma chambers are located on either side of the dyke. Compared to their original models, we focus merely on an opening dyke without shear components. This scenario corresponds to our Model DI, where the dyke has been modelled with Method 2, in Section 2.2.

The discrepancies computed for CS1-3 (Table 3) are in good agreement with our previous results. In Model CS2, as in Model C, both surface (ϵ) and maximum discrepancies (Ξ) are negligible (<5 per cent). Models CS1 and CS3 have a set of geometrical and physical parameters more complex than Models A and D1, henceforth producing a different, more intricate, deformation pattern (see e.g. Fig. A-7a). However, as expected from Model A and DI results, Model CS1 discrepancies are weaker than Model CS3 discrepancies. In Model CS1, analytical and FEM solutions fit closely, with the exception of the near-field vertical displacements. Henceforth, the surface and horizontal ($\Xi_x|_{\min}$ and $\Xi_x|_{\max}$) discrepancies of Model CS1 are insignificant, but $\Xi_z|_{\max}$ are significant and reach 18.5 per cent. In Model CS3, horizontal and vertical surface discrepancies are up to 20 per cent, and reflect how the analytical and FEM solutions differ by 10–15 per cent over a 10 km^2 area encompassing the three sources, with maxima of 25 per cent for U_z and U_x above or slightly offset of the spherical sources, respectively (see also Fig. A-7b and c).

For both models CS1 and CS3, the significant discrepancies calculated contrast with the negligible discrepancies calculated for

Table 3. Geometry, physical parameters and discrepancies obtained for Models CS1-3 (Fig. 11 and Fig. A-7). Parameters are adapted from Elsworth *et al.* (2008), Linde *et al.* (2010) and Wright *et al.* (2006) for the volcanic plumbing system of Soufrière Hills Volcano, Montserrat, West Indies and from Wright *et al.* (2006) for the magmatic system of the Dabbahu-Gab'ho segment, Afar, Ethiopia. Overpressures are either given in the referenced works or, where indicated, derived from the source volume change (Delaney & McTigue 1994). In CS3, we chose a common value of 1 km for the magma chambers radius, otherwise unknown. Young's modulus value is taken from Hamling *et al.* (2010). In the FE model, dykes are modelled with Method 2, described in Section 2.1.

		Model CS1	Model CS2	Model CS3
Mogi source 1	Centre position (km)	(0,0,−6)	(0,0,−5)	(3,6.5,−5)
	radius (km)	1	0.5	1
	$\Delta P1$	9.29 MPa	−2.5 MPa	−2.03 GPa
	$\Delta V1$ (km^3)	0.03		−0.2
Mogi source 2	Centre position (km)	(0,0,−12)	n/a	(−4,−1,−5)
	radius (km)	1	n/a	1
	$\Delta P2$	51.25 MPa	n/a	−3.06 GPa
	$\Delta V2$ (km^3)	−0.16		−0.3
Okada source	Centre position (km)	n/a	(0,0,−2.85)	(0,0,−5.5)
	width × height (km)	n/a	2.9 × 1	12 × 7
	Opening (m)	n/a	0.16	8
Source separation (radii)		6	1.4	Mogi1-Ok.:: 4 Mogi2-Ok.:: 3
Crustal properties	E (GPa)	2.5	10	80
	ν 0.25	0.25	0.25	
Discrepancies (per cent)	ϵ_x	3.3	0.9	20.7
	ϵ_y	3.2	0.6	17.50
	ϵ_z	3.2	1.9	20.8
	$\Xi_x\|_{\min}$	0.1	2.2	2.4
	$\Xi_x\|_{\max}$	0.0	0.6	10.3
	$\Xi_z\|_{\min}$	2.4	1.0	13.7
	$\Xi_z\|_{\max}$	18.5	1.8	16.0

Models A and DI with similar source separations. This is particularly due to the 8 m opening of the dyke in CS3, against only 1 m in Model DI, and to the high, if not unrealistic, overpressures applied on most of the magma chambers walls in the two case studies. In Model CS3, we chose a typical magma chamber radius of 1 km and calculated the overpressure from the volume change given in Wright *et al.* (2006), and from the relation between radius, pressure and volume changes given in Delaney & McTigue (1994), where pressure and radius are inversely proportional. Increasing the magma chambers radii would induce a trade-off between decreasing the source interaction by decreasing the overpressure applied, and increasing the source interaction as the sources would grow closer.

3.5 Summary

It is difficult to deduce a general law for the discrepancies between analytical and FE solutions valid for all the geometries and parameters investigated. Nevertheless, we can extract the following findings from our models:

(i) The discrepancies induced when aligning and superposing a Mogi and an Okada source in Models C and DII (Fig. 2) are always negligible (<5 per cent).

(ii) In contrast, models with superposed or juxtaposed Mogi sources (Models A and B) and models with juxtaposed Mogi and Okada sources (Models DI) result in analytical solutions differing from the numerical solution by up to 16, 14 and 300 per cent, respectively. For these three models, the discrepancies are maximal when the sources are the closest, in which case they are significant up to a horizontal distance of up to 5 km. All surface and maximum discrepancies computed for Models A and B become negligible when the sources are separated by 4 radii or more (Figs 4–8).

(iii) For model DI, in the case where the dyke opening is modelled with relative displacements of the dyke walls (Method 2) or pressure difference (Method 3), all discrepancies become insignificant for a source separation of more than 3 radii. However, when applying fixed displacements (Method 1), the discrepancies are significant for a source separation of at least 9 radii.

(iv) When applying our methodology to three case studies adapted from the magmatic systems of Soufrière Hills Volcano, Montserrat, West Indies (Models CS1-2) and the Dabbahu segment, Afar, Ethiopia (Model CS3), we find discrepancies in good agreement with the above results. Additionally, these models highlight how the source interaction and the discrepancies are related to the trade-off between overpressure and radius.

4 MAPPING THE DISCREPANCIES INTO MODEL PARAMETERS ΔP, DYKE OPENING, AND SOURCE SEPARATION (MODEL A AND DI)

4.1 Sensitivity analysis

Data sets of ground deformation are often inverted for geophysical model parameters, such as magma chamber pressure and volume,

Table 4. Summary of parameters and discrepancies for Models A-G1'a and DIa used as references in the sensitivity analysis tests (Figs 12 to 15). The results of the corresponding Monte-Carlo inversions are listed in Table 5. The domain elastic parameters are $E = 10$ GPa and $\nu = 0.25$.

		Model A-G1'a	Model DIa		
			Method 1	Method 2	Method 3
Mogi source 1	Centre position (km)	(0,0,−5)		(0.75,0,−2.5)	
	radius (km)	0.5		0.5	
	$\Delta P1$ (MPa)	20		−20	
Mogi source 2	Centre position (km)	(0,0,−6.25)		n/a	
	radius (km)	0.5		n/a	
	$\Delta P2$ (MPa)	20		n/a	
Okada source	Centre position (km)	n/a		(0,0,−2.5)	
	width × height (km)	n/a		1 × 1	
	Opening (m)	n/a	1	1	n/a
	ΔP (MPa)	n/a	n/a	n/a	12
Source separation (radii)		2.5		1.5	
Discrepancies (per cent)	ϵ_x	11.6	553.7	24.1	11.1
	ϵ_y	11.4	9.8	7.6	15.5
	ϵ_z	14.1	22.5	6.8	11.9
	$\Xi_x\|_{\min}$	8.1	298.8	8.7	17.6
	$\Xi_x\|_{\max}$		185.1	0.5	2.7
	$\Xi_z\|_{\min}$	15.5	5.3	7.0	12.9
	$\Xi_z\|_{\max}$		n/a	n/a	n/a

as well as its location. Therefore, we investigate in the following section how the estimation of model parameters is affected by neglecting the source interaction when two analytical models are combined, or in other words how the neglected source interaction is mapped into model parameters. As a reference, we use the numerical solutions of Model A-Group G1'a or Model DIa. In Model A-Group G1'a, two spherical sources with radius $a = 500$ m are superposed (upper source $a/d = 0.1$) while in Model DIa the 500 m radius spherical source is juxtaposed to a 1 km × 1 km dyke opening by 1 m (see Table 4 for a list of the corresponding model parameters). We vary in the combined analytical model either the source separation, the Mogi source pressurization $\Delta P1$ or $\Delta P2$ (Fig. 12), or the dyke opening in order to match the numerical reference model (Fig. 15 for Method 3, and Figs 13 and 14 for Methods 1–2). This match is quantified by the discrepancies as defined in Section 2.3 (eqs 1 and 2). We plot a grid of the discrepancies ϵ and Ξ as well as the mean of ϵ, calculated for a range of each of the three parameters. Red areas correspond to negligible discrepancies hence to a best fit between the numerically generated data set (reference model) and the analytical combined model. The vertical red line indicates the parameter values of the reference numerical model, which the analytical models aim to retrieve. In this way, we can quantify how the interaction of deformation sources, neglected by the analytical models, maps into distorted model parameters. By varying one model parameter at the time, we assess the sensitivity of the model solution to this model parameter.

The sensitivity analysis of Model A-Group G1'a (Fig. 12) shows that the discrepancies we try to minimize are, for the range of values chosen, less sensitive to the source separation than to the overpressure in the spherical sources, particularly for the shallower source ($\Delta P1$). Compared to the reference model, the discrepancies map into incorrect model parameters where $\Delta P1$ is underestimated by 10–20 per cent, $\Delta P2$ by 20–35 per cent, and the source separation is overestimated by 70–100 per cent. The fact that the red gridpoints, calculated for the various discrepancies, overlap, indicates that the solution of the respective model parameter satisfies all components of the surface displacement.

The sensitivity analysis of Model DIa (dyke juxtaposed to chamber) is represented in Fig. 15 for a dyke modelled with Method 3, and in Figs 13 and 14 for a dyke modelled with Method 1 and 2, respectively:

(i) *Method 1:* The high discrepancies throughout Fig. 13 demonstrate that no analytical model was found fitting the reference numerical surface displacements. The mean surface discrepancies are systematically larger than 70 per cent, dominated by ϵ_x larger than 100 per cent. Taken separately, the minima for ϵ_y and ϵ_z are still between 6 and 25 per cent, and would yield a dyke opening underestimated by up to 50 per cent, a source separation overestimated by up to 45 per cent, but a reasonable ΔP only 5 per cent off its actual value (Table 4). The large values of $\Xi|_{\min}$ or $\Xi|_{\max}$ (e.g. $\Xi_x|_{\max} > 150$ per cent) emphasize how strongly the analytical and numerical surface displacements differ, and that combining a Mogi and Okada solutions can never represent a scenario that we modelled through Method 1, where the dyke is fixed and the magma chamber accounts for all the deformation triggered by the interacting sources.

(ii) *Method 2:* Compared to the previous method, the dyke modelled with Method 2 can now be deformed remaining at a constant opening of 1 m. In this case, the results depicted in Fig. 14 show that an inversion using the analytical models would lead to an underestimation of the dyke opening by 20 per cent and to an incorrect estimation of ΔP and source separation by up to 10 per cent, with a minimum mean(ϵ) of 10 per cent. For the parameter range given, the spread of the smaller discrepancies points out that the model is more sensitive to the dyke opening than to ΔP, and finally to the source separation.

(iii) *Method 3:* When the numerical model is realized by a tabular crack (Method 3), the volume change of the numerical pressurized crack is equivalent to the volume change of an Okada source of same dimensions and opening by 1 m. An inversion using the analytical

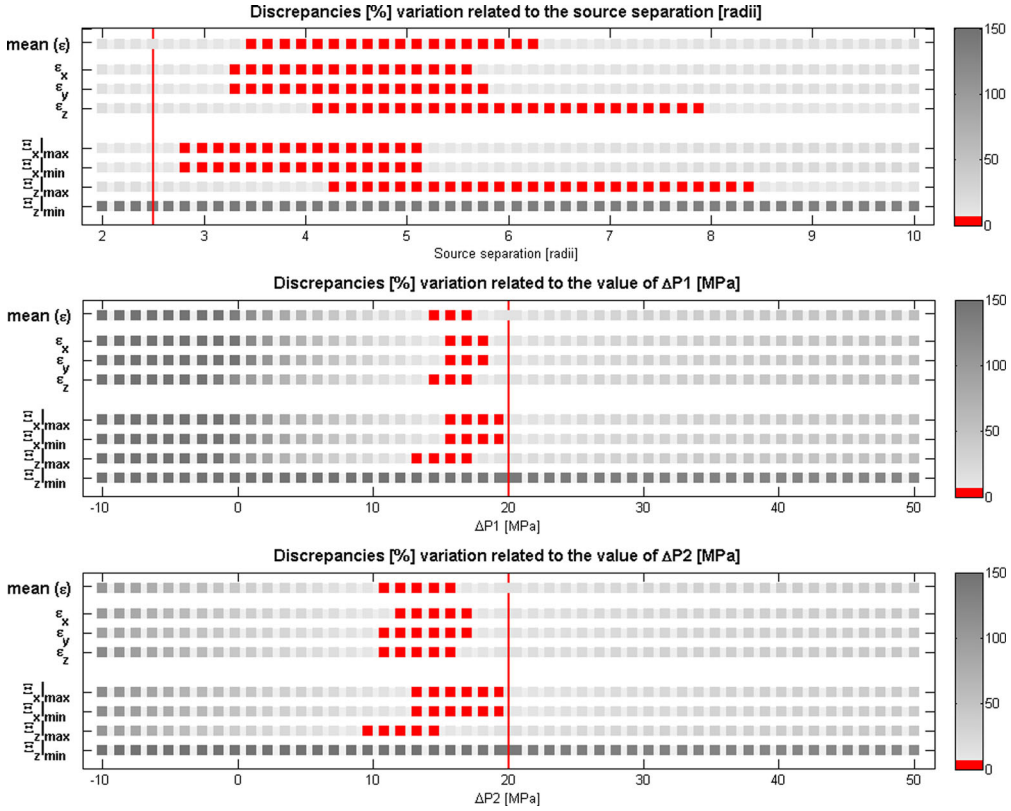

Figure 12. Sensitivity analysis for a model with two superposed Mogi sources of radii $a = 500$ m and upper source radius-over-depth ratio $a/d = 0.1$ (Model A-G1'a). The numerical solution is taken as reference and in the analytical model we vary either the source separation, $\Delta P1$, or $\Delta P2$ (from top to bottom panel). The red lines indicate the position of the reference model parameters (here A-G1'a). Reading each panel horizontally, the colour code refers to the value of the surface discrepancies (ϵ), their mean, and of the discrepancies at the extrema (Ξ). Values in red are discrepancies below 5 per cent and indicate a good fit between the analytical and reference models. Reading the panels vertically gives an estimate of each discrepancy component for a given model parameter, indicating their respective sensitivity. Note that $\Xi_x|_{\min} = \Xi_x|_{\max}$ due to symmetry. Additionnally, the FEM $U_z|_{\min}$ tend to zero hence $\Xi_z|_{\min}$ results will not be taken into account. The parameter ranges showing the best-fit to the numerical model are listed in Table A-6.

models points to a source pressurization and a dyke opening within 10 and 20 per cent of their actual value, respectively, and a source separation overestimated by up to 25 per cent (Fig. 15). The minimum mean (ϵ) and ϵ are approximately equal to 7 per cent. As for Method 2, the various discrepancies computed for Method 3 indicate that the model solution is more sensitive to a variation in dyke opening and ΔP, but less sensitive to a change in source separation.

To summarize, when modelling a magmatic system composed of two Mogi sources, neglecting the source interaction ultimately leads to a significant underestimation of pressurization and vast overestimation of the source separation if the original sources are as close as 2.5 radii.

When modelling a magmatic system composed of a dyke juxtaposed to a magma chamber (Model DI), the discrepancies are enormous when Method 1 is employed. This is due to the fact that the dyke is fixed in space and the 'interaction' between the two sources results in the deformation of the spherical source only, while the dyke acts as a rigid, pinned, barrier. When comparing the reference numerical model using Method 2 or 3, the discrepancies are much smaller and tend to be more sensitive to a variation in dyke opening and ΔP, but less sensitive to source separation. When using Method 2, neglecting the source interaction is likely to lead to an underestimation of the dyke opening by up to 20 per cent and to give a comparatively better estimate of the source pressurization and the distance between sources. With Method 3, the discrepancies calculated for each parameter range indicate stronger dissimilarities between the numerical and analytical solutions than with Method 2. Given that Method 3 is the closest to a realistic pressurized dyke, the discrepancies between Method 3 and analytical solutions provide a measure of the error made when a real dyke is modelled with a constant-opening dislocation.

4.2 Inversions

While the 'grids' in Figs 12 and 15 give some valuable insight into how each of the deformation components contributes to the estimation of a model parameter such as ΔP, source separation and dyke opening, a common inversion scheme will seek to minimize the misfit between input and model in all components simultaneously. Therefore, we take the scenarios of Model A-Group G1' and DIa and use their respective FE surface displacements as input data for the parameter inversion based on the solution of Mogi and Okada. In other words, we assume that the FE solutions represent the displacement fields for real cases where magma sources close to each other interact, and estimate how strongly this interaction affects the retrieval of the model parameters by inversion with analytical models. We employ a hybrid Monte Carlo, downhill simplex inversion scheme (Clarke 1996; Wright *et al.* 1999) to estimate volume change, dyke opening and source location. With this method, calculation of the L2-norm allows to find the minimum misfit between the FE input and the analytically modelled displacements. To make sure the parameters retrieved do not correspond to local

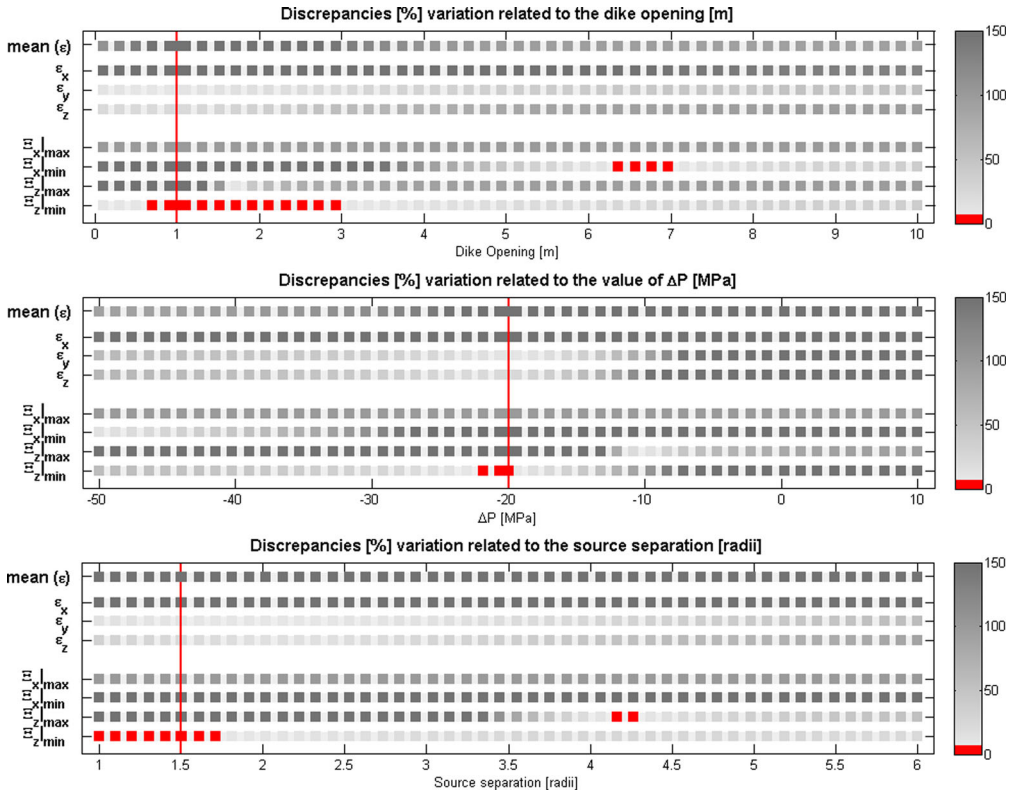

Figure 13. Sensitivity analysis for a model of a dyke opening by 1 m, modelled with Method 1, juxtaposed to a deflating spherical source ($\Delta P = -20$ MPa). The sources are separated by a distance of 1.5 radii (Model DI -M1a). The numerical solution is taken as reference and in the analytical model we vary either the source separation, $\Delta P1$, or $\Delta P2$ (from top to bottom panel). The red lines indicate the position of the reference model parameters (here A-G1'a). Reading each panel horizontally, the colour code refers to the value of the surface discrepancies (ϵ), their mean, and of the discrepancies at the extrema (Ξ). Values in red are discrepancies below 5 per cent and indicate a good fit between the analytical and reference models. Reading the panels vertically gives an estimate of each discrepancy component for a given model parameter, indicating their respective sensitivity. In this model the FEM $U_x|_{\max}$ tend to zero hence $\Xi_x|_{\max}$ results will not be taken into account. The parameter ranges showing the best-fit to the numerical model are listed in Table A-6.

minima, we restart the inversion 2000 times with 200 randomly chosen starting parameter values. As previously, the full domain of the FE models are 200 km × 200 km × 100 km for Model A and 110 km × 100 km × 35 km for Model DI, in order to avoid including FEM boundary effects in the solution. However, we invert for all models the FE displacements only in a 30 km × 30 km area in the centre of the models. The dimensions of this area corresponds to the spatial extension of GPS or InSAR data used during inversions. The source parameters inverted for are indicated in bold in Table 5. In Inversions #1, #2 and #3, we have tried to retrieve only one source parameter: the dyke position, the dyke opening, and the magma chamber volume change, respectively (Model DI), or the deeper magma chamber position (Source 2), Source 2 volume change, and Source 1 volume change, respectively (Model A). In Inversions #4, we have jointly inverted for dyke opening and magma chamber volume change (Model DIa), or the two magma chambers volume change (Model A). In inversions #5, we have tried to retrieve the positions of both sources together with the volume changes of the magma chamber(s) (Model A) and the dyke opening (for Model DI). For Model DI (numerical Method 2), whether independently or jointly inverted for, the source deflation ΔV (hence ΔP) is similar to its reference value, and the dyke opening and the source separation are only slightly under- or overestimated, respectively (Table 5).

For Model A, we have run the inversions with source separation between 2.5 and 10 radii for the numerical model with interacting sources (rows a–f in Table 5). We also have added the individual FE displacements generated by each of the sources for all source separations, and we have inverted the sum, in the following referred to as 'M1+M2'. This sum is identical to the analytical solution except for the noise introduced by the FE method (see 'M1+M2' in Table A-1). As a reference, we have furthermore inverted the sum of the analytical solutions for the same set of model parameters. In this case, the inversions have retrieved the original parameters, pointing out the fact that only the numerical noise introduced by the FE method affects the results of inversions of the 'M1+M2' solutions. Finally, in order to evaluate if ours findings can be generalized and if they are applicable to 'real' deformation field and associated analytical inversions, we perform a statistical study and give the errors on the source parameters retrieved during an analytical inversion of 100 synthetic data sets of the 'full' (Model A-G1') and the 'summed' ('M1+M2') solutions for two superposed spherical sources separated by 2.5–10 radii. The data sets are generated adding to the original solutions Gaussian noise with a standard deviation equal to 1 cm, equivalent to data noise in GPS measurements, for instance. We then applied a bootstrap method, commonly used for deformation data sets, to obtain the final resampled synthetic data sets with added noise (Efron & Tibshirani 1986; Gottsmann *et al.* 2006; Lisowski 2007; Foroozan *et al.* 2010).

In Fig. 16, we compare the normalized error between reference and retrieved parameters for both interacting and non-interacting source solutions in Inversions #1–4, along with the distribution of errors given by the statistical tests. This figure therefore highlights how the results of the inversions are affected both by neglecting

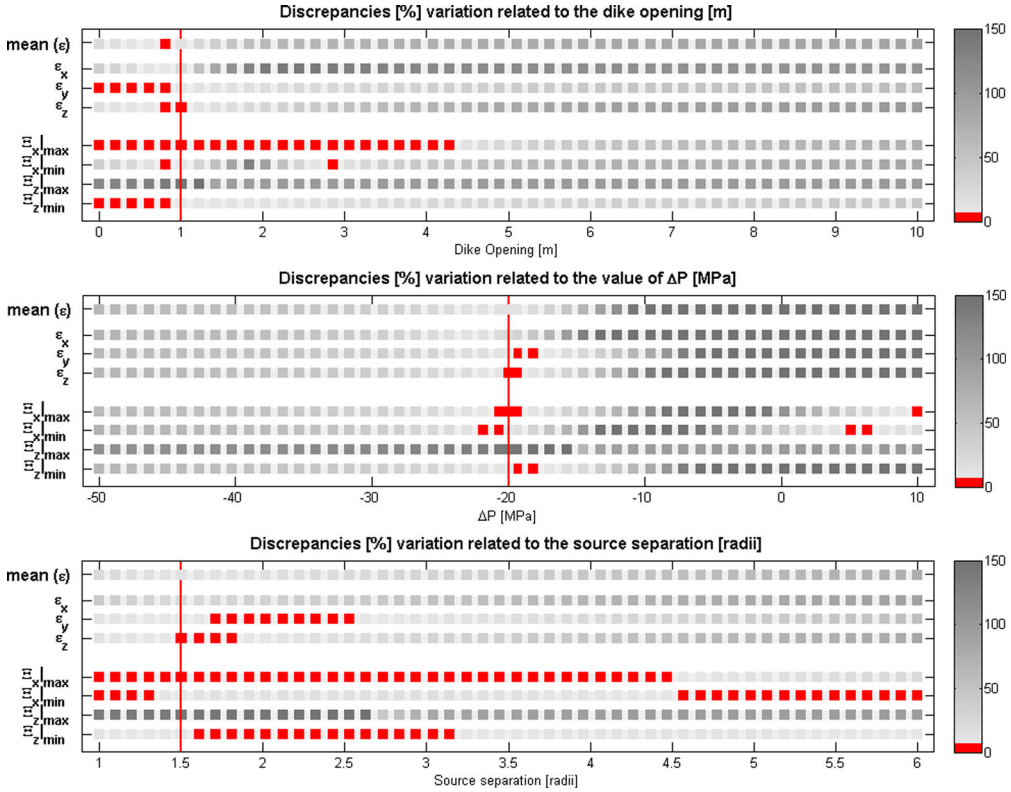

Figure 14. Sensitivity analysis for a model of a dyke opening by 1 m, modelled with Method 2, juxtaposed to a deflating spherical source ($\Delta P = -20$ MPa). The sources are separated by a distance of 1.5 radii (Model DI-M2a). The numerical solution is taken as reference and in the analytical model we vary either the source separation, $\Delta P1$, or $\Delta P2$ (from top to bottom panel). The red lines indicate the position of the reference model parameters (here A-G1'a). Reading each panel horizontally, the colour code refers to the value of the surface discrepancies (ϵ), their mean, and of the discrepancies at the extrema (Ξ). Values in red are discrepancies below 5 per cent and indicate a good fit between the analytical and reference models. Reading the panels vertically gives an estimate of each discrepancy component for a given model parameter, indicating their respective sensitivity. In this model the FEM $U_x|_{\max}$ tend to zero hence $\Xi_x|_{\max}$ results will not be taken into account. The parameter ranges showing the best-fit to the numerical model are listed in Table A-6.

the surface interaction and by noise contamination. Overall, the influence of the source interaction on the retrieved parameters is significant until a minimum source separation of 8 radii is reached. When all but one parameters are fixed (Inversions #1–3 in Figs 16a, c and d), the error for the 'M1+M2' parameters retrieved from the non-noisy solution only reach ±2 per cent. The inversions results are in realistic ranges, but are affected by large or very large errors, in particular when one inverts for the depth of the deep source. The results for the full, non-noisy, FE model confirm our previous results underestimating ΔV, hence ΔP, by up to 30 per cent and overestimating the source separation by up to 20 per cent. The results obtained in the statistical studies are consistent with those results. When inverting for only one parameter, the depth of the lower source, that is the source separation, is overestimated by up to 16 per cent ($\sigma \approx 2$ per cent), its volume change is in average underestimated by up to 23 per cent ($\sigma \approx 3$ per cent) and the volume change of the upper source is in average underestimated by as much as 16 per cent ($\sigma \approx 2$ per cent). When the source parameters were retrieved within 5 per cent for source separation of more than 4 radii, here the comparison between full and summed solution shows that the source interaction can still introduce bigger errors, of up to 17 per cent ($\sigma \approx 4$ per cent), at this distance. If the errors on the source parameters decrease with the source separation, however, when the sources are separated by more than 8 radii, the errors average and standard deviation on the lower source depth and volume change are again unexpectedly high, for both full and summed solution. This demonstrates that, as the lower source is getting deeper and its effect on the surface deformation lessens, retrieving its parameters is difficult, particularly because of the introduction of the noise.

When $\Delta V1$ and $\Delta V2$ are simultaneously inverted for (Inversion #4, Figs 16e and f), neglecting the interaction between sources lead, when inverting the original non-noisy solutions, to underestimating the volume change of the upper source by 30 per cent while overestimating the lower volume change by 20 per cent when the distance between sources is 2.5 radii. When the sources are further apart, the two volume changes can be retrieved with 5 per cent. When depths and ΔV are jointly inverted for (Inversion #5, Fig. 16c), results are unrealistic for small source separation (<4 radii) and still incorrectly estimated until 8 radii, when all parameters are retrieved within ±10 per cent. This indicates that even small uncertainties in deformation data (produced by the FE method, in these original data sets) can lead to unrealistic source parameters if the inversion is based on source models which are in close vicinity to each other. This is confirmed for both Inversions #4 and #5, where the average errors and standard deviation on the source parameters when inverting the noisy resampled data set are large and insignificant, due to the fact that the inversion scheme tries to retrieve an overall ΔV and depth z consistent with the surface displacements, rather than solving for the individual ΔV_1 and ΔV_2, z_1 and z_2.

In order to understand why source interaction affects heavily the inversion results, we have plotted the surface displacement solutions for different source separation in Fig. 17, where we compare FEM and analytical models. The curves corresponding to the analytical

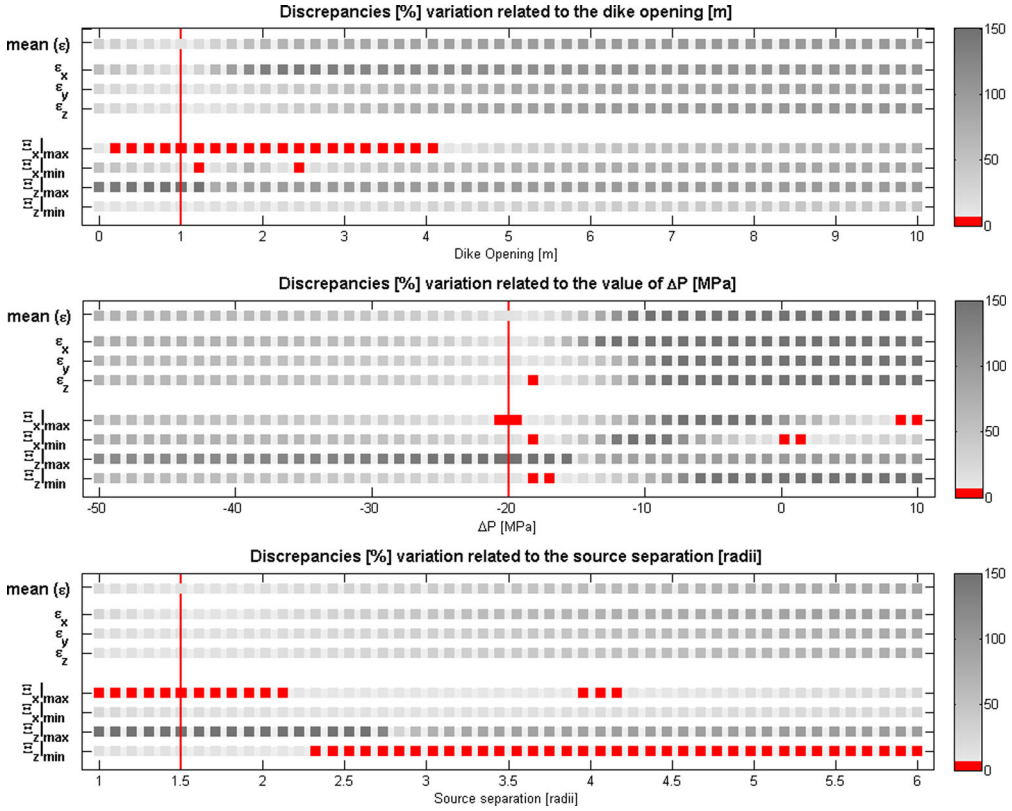

Figure 15. Sensitivity analysis for a model of a dyke opening by 1 m, modelled with Method 3, juxtaposed to a deflating spherical source ($\Delta P = -20$ MPa). The sources are separated by a distance of 1.5 radii (Model DI-M3a). The numerical solution is taken as reference and in the analytical model we vary either the source separation, $\Delta P1$, or $\Delta P2$ (from top to bottom panel). The red lines indicate the position of the reference model parameters (here DI-M3a). Reading each panel horizontally, the colour code refers to the value of the variation of surface discrepancies (ϵ), their mean, and of the discrepancies at the extrema (Ξ). Values in red are discrepancies below 5 per cent and indicate a good fit between the analytical and reference models. Reading the panels vertically gives an estimate of each discrepancy component for a given model parameter, indicating their respective sensitivity. In this model the FEM $U_x|_{\max}$ tend to zero hence $\Xi_x|_{\max}$ results will not be taken into account. The parameter ranges showing the best-fit to the numerical model are listed in Table A-6.

solutions are well separated from each other and progressively less peaked for increasing source separation, while the numerical solutions overlap, or even show an inversion in the curve progression, for source separation up to 5–8 radii. This shows how source interaction induces a strong component of non-uniqueness to the displacement field.

5 SUMMARY AND CONCLUSIONS

In this study, we have evaluated the limits of combining Mogi and Okada analytical sources for several model scenarios, comparing the analytical surface displacements with the equivalent numerical model solutions, which also account for the source interaction. We have carried out a series of synthetic tests combining either two spherical sources representing magma chamber models, or a magma chamber and an adjacent dyke model. As model parameters we have used the relative source positions, dyke opening and the source pressurization.

We have modelled numerically the Mogi source by embedding a pressurized cavity (corresponding to a fluid-filled magma chamber) into a large numerical domain representing a half-space. To model numerically the Okada source, we tested three approaches: applying a constant normal displacement on the dyke walls (Method 1); imposing a constant displacement on one of the dyke walls with respect to the other (Method 2) and applying a pressure normal to the dyke walls (Method 3). To quantify the discrepancies between analytical and numerical solutions, we have estimated the differences in the surface displacements either by considering the entire surface (ϵ) or by examining the difference at the extrema of the surface displacement (Ξ).

We have demonstrated that discrepancies are negligible for all models with superposed or aligned dyke and magma chamber (Models C and DII). However in all other cases tested, neglecting the source interaction introduces significant discrepancies whose magnitude depends on the source type, model geometry and on the source strength (pressurization or dyke opening). FE and analytical models differ the most in the near field, where volume or pressure estimates of magma intrusions are dominated by large amplitudes. The discrepancies decrease with increasing source separation, yet number and diversity of the parameters involved prevent the derivation of a simple mathematical expression to estimate these discrepancies. Instead we employ numerical models and consider several scenarios separately.

Amongst these scenarios, we have found that when two pressurized sources are either superposed (Model A) or juxtaposed (Model B) they interact, for example, by shielding each other if they are both inflating. Neglecting this interaction causes discrepancies of up to 16 per cent at 2.5 radii source separation, which become negligible for a source separation of more than 4 radii. Depending on the pressurization of the sources (inflation or deflation), and on their position, the analytical models either under- or overestimate the surface displacements (Figs 6 and 9).

Table 5. Inversions of the synthetic data sets (numerical reference model) using combined analytical models corresponding to Models A-G1'a-f, and DIa. In Model A, two spherical sources of radius $a = 500$ m, and pressurized by $\Delta P1 = \Delta P2 = 20$ MPa, are superposed by a distance of 2.5 (G1'a) to 10 radii (G1'f). In Model DI, a 1 km × 1 km dyke opening by 1 m is juxtaposed by 1.5 radii (i.e. 750 m) to a deflating source ($\Delta P = -20$ MPa). Note that inversions #1 through #3 retrieve only one parameter (in bold) while inversions #4 and #5 attempt to obtain several parameters simultaneously.

	Source parameters		Reference model	Inversions # #1	#2	#3	#4	#5
DIa (M2)	Mogi	ΔV (10^{-3} km^3)	−1.9	−1.9	−1.9	**−1.9**	**−1.9**	**−1.9**
	source	ΔP (MPa)	−20.0	−20.0	−20.0	−19.7	−18.9	−19.0
		x (m)	750	750	750	750	750	**744**
	Okada	Opening (m)	1	1	**0.72**	1	**0.68**	**0.70**
	source	x (m)	0	**-238**	0	0	0	**−178**
	Source separation (radii)		1.5	**1.97**	1.5	1.5	1.5	**1.84**
	Mogi	ΔV_1 (10^{-3} km^3)	1.9	1.9	1.9	**1.6**	**1.4**	**3.8**
	source 1	ΔP_1 (MPa)	20.0	20.0	20.0	16.4	13.9	38.2
		depth (km)	5.00	5.00	5.00	5.00	5.00	**5.72**
A-G1'a	Mogi	ΔV_2 (10^{-3} km^3)	1.9	1.9	**1.4**	1.9	**2.3**	**-1.2×10^{14}**
	source 2	$\Delta P2$ (MPa)	20.0	20.0	14.8	20.0	23.6	-1.2×10^{15}
		depth (km)	6.25	**7.42**	6.25	6.25	6.25	**2.70×10^{8}**
	Source separation (radii)		2.5	**4.8**	2.5	2.5	2.5	**5.4×10^{8}**
	Mogi	ΔV_1 (10^{-3} km^3)	1.9	1.9	1.9	**1.7**	**1.6**	**−25.2**
	source 1	ΔP_1 (MPa)	20.0	20.0	20.0	17.7	16.8	−256.4
		depth (km)	5.00	5.00	5.00	5.00	5.00	**5.09**
A-G1'b	Mogi	ΔV_2 (10^{-3} km^3)	1.9	1.9	**1.6**	1.9	**2.1**	**28.7**
	source 2	$\Delta P2$ (MPa)	20.0	20.0	16.5	20.0	21.4	292.7
		depth (km)	6.50	**7.26**	6.50	6.50	6.50	**5.14**
	Source separation (radii)		3.0	**4.5**	3.0	3.0	3.0	**5.1**
	Mogi	ΔV_1 (10^{-3} km^3)	1.9	1.9	1.9	**1.9**	**1.9**	**2.8**
	source 1	ΔP_1 (MPa)	20.0	20.0	20.0	18.9	18.9	29.1
		depth (km)	5.00	5.00	5.00	5.00	5.00	**5.38**
A-G1'c	Mogi	ΔV_2 (10^{-3} km^3)	1.9	1.9	**1.8**	1.9	**2.0**	**0.8**
	source 2	$\Delta P2$ (MPa)	20.0	20.0	18.1	20.0	20.0	8.5
		depth (km)	7.00	**7.40**	7.00	7.00	7.00	**7.53**
	Source separation (radii)		4.0	**4.8**	4.0	4.0	4.0	**4.3**
	Mogi	ΔV_1 (10^{-3} km^3)	1.9	1.9	1.9	**1.9**	**1.8**	**2.1**
	source 1	ΔP_1 (MPa)	20.0	20.0	20.0	19.4	18.6	21.2
		depth (km)	5.00	5.00	5.00	5.00	5.00	**5.12**
A-G1'd	Mogi	ΔV_2 (10^{-3} km^3)	1.9	1.9	**1.8**	1.9	**1.9**	**1.7**
	source 2	$\Delta P2$ (MPa)	20.0	20.0	18.8	20.0	19.7	17.3
		depth (km)	7.50	**7.75**	7.50	7.50	7.50	**7.34**
	Source separation (radii)		5.0	**5.5**	5.0	5.0	5.0	**4.4**
	Mogi	ΔV_1 (10^{-3} km^3)	1.9	1.9	1.9	**1.9**	**2.0**	**1.8**
	source 1	ΔP_1 (MPa)	20.0	20.0	20.0	19.8	20.0	18.0
		depth (km)	5.00	5.00	5.00	5.00	5.00	**4.92**
A-G1'e	Mogi	ΔV_2 (10^{-3} km^3)	1.9	1.9	**1.9**	1.9	**1.9**	**2.0**
	source 2	$\Delta P2$ (MPa)	20.0	20.0	19.4	20.0	19.4	20.6
		depth (km)	9.00	**9.16**	9.00	9.00	9.00	**8.32**
	Source separation (radii)		8.0	**8.3**	8.0	8.0	8.0	**6.8**
	Mogi	ΔV_1 (10^{-3} km^3)	1.9	1.9	1.9	**1.9**	**2.0**	**1.9**
	source 1	ΔP_1 (MPa)	20.0	20.0	20.0	19.8	20.0	19.20
		depth (km)	5.00	5.00	5.00	5.00	5.00	**4.97**
A-G1'f	Mogi	ΔV_2 (10^{-3} km^3)	1.9	1.9	**1.9**	1.9	**1.9**	**1.9**
	source 2	$\Delta P2$ (MPa)	20.0	20.0	19.4	20.0	19.3	19.3
		depth (km)	10.00	**10.17**	10.00	10.00	10.00	**9.48**
	Source separation (radii)		9.0	**10.3**	9.0	9.0	9.0	**9.0**

Additionally, we have found that the discrepancies computed are overall similar for a particular model geometry and source pressurization, regardless of the radius-over-depth ratio (a/d) or the use of McTigue's expression for a finite source. Surprisingly, the results obtained for the various pressurization values listed in Table 2, specifically the equivalent discrepancies for the same ratio $\Delta P1/\Delta P2$, also reveal that the discrepancies are not pressure-dependent, unlike the surface displacements due to an individual source. In conclusion, the discrepancies depend on the proximity of interacting surfaces rather than on the strength of the deformation sources. Hence, in order to avoid closely spaced deformation sources, one could decrease their radius and therefore increase the

Table 6. Inversion #1–5, Model A-G1'a (2.5 radii separation): normalized errors on the parameters retrieved when inverting the synthetic (FE) solution and distribution of the errors. An additional Gaussian noise with standard deviation 1 cm was added to the numerical solution, which has been then bootstrapped. The mean, the standard deviation (σ), the minimum and the maximum error on each parameters are given for each Inversions of the 'full' solution of Model A, and of the summed 'M1+M2' solution and relative parameters to which was added some Gaussian noise and bootstrapped. The errors distribution is also represented in Figs 16 and A-8

Inversions			A-G1'	Distribution of errors			
				Mean	σ	Min.	Max.
'Full' solution	#1	z_2	18.8	16.2	2.3	10.4	22.7
	#2	ΔV_2	−26.1	−23.1	2.7	−30.4	−15.9
	#3	ΔV_1	−18.2	−16.2	1.9	−21.3	−11.2
	#4	ΔV_1	−30.5	−32.2	19.3	−78.1	−32.2
		ΔV_2	17.8	22.9	28.1	−41.4	88.1
	#5	ΔV_1	91.0	−1235.6	2540.1	−7451.5	7653.6
		Δz_1	14.4	10.7	22.4	-31.2	63.7
		ΔV_2	-6.1×10^{15}	1197.7	2526.2	−7699.7	7427.0
		Δz_2	-4.3×10^{9}	−52.0	46.7	−99.1	34.5
Summed 'M1+M2'	#1	z_2	0.5	3.8	2.4	−2.7	9.0
	#2	ΔV_2	−1.1	−4.9	3.8	−13.3	7.3
	#3	ΔV_1	−0.7	−3.8	2.6	−9.6	4.4
	#4	ΔV_1	2.9	−37.5	23.0	−102.1	21.1
		ΔV_2	−5.2	48.4	32.8	−26.0	140.6
	#5	ΔV_1	−93.9	−1761.4	3602.6	−7538.4	6809.6
		Δz_1	−25.3	−1815.2	2284.1	−7694.3	2721.1
		ΔV_2	89.6	34.1	34.1	−95.3	85.7
		Δz_2	−10.9	1746.4	2250.1	−2788.5	7602.2

distance between the interacting surfaces, while maintaining the same strength by increasing the pressure, due to the trade-off between radius and pressure change ($a^3\Delta P$, Mogi, 1958). However, this relationship implies that a small change in the radius must be compensated by a large increase in pressure. Although not shown here, the discrepancies are also independent of a variation of the Young's modulus E of the surrounding medium (as long as the medium is homogeneous). This is because both sources are affected in the same manner.

In models with juxtaposed dyke/magma chambers (Model DI), neglecting the source interaction can also lead to significant discrepancies in surface displacements, which, however, depend strongly on the approach taken to model the dyke numerically. Although Methods 1–3 give identical surface displacements when the dyke is the only source in the FE model and is deep enough, the variations in the discrepancies obtained when two sources are combined, emphasize that each method models a dyke with a different physical behaviour and which interacts in a different way with the spherical source.

Method 1, limited to vertical dykes, may correspond to a dyke embedded in a large, very stiff region of the half-space, such as a large pluton formed by multiple cooled intrusions, which would react very rigidly to the stress exerted by a spherical magma chamber located in a much more compliant region adjacent to the pluton. Of course, modelling deformation sources embedded in such heterogeneous medium with the analytical Okada solution leads to large discrepancies (>550 per cent).

In contrast to Method 1, both Method 2 and Method 3 represent a non-rigid dyke, which can absorb a part of the deformation field due to the combined sources. In Method 3, the static dyke is subjected to a uniform internal pressure. When no other source is present, the regional stress is also uniform and the dyke cross section is elliptical, as predicted by the equations of elasticity (Pollard & Muller 1976). However, it opens asymmetrically when another source is present and, as with Method 2, the dyke is either 'pushed away' from the spherical source when it is inflating, or 'pulled' towards it when it is deflating. The discrepancies induced when neglecting this deformation are up to 25 and 18 per cent for Methods 2 and 3, respectively, and become negligible beyond 3 radii separation. The discrepancies summarized in Table 2, generally smaller for Method 2 than for Method 3, suggest that in this source configuration the Okada source can represent a flexible dyke when it is further than 3 radii from the Mogi source.

In the case of one juxtaposed opening Okada and one deflating Mogi source, an inversion of the surface displacements computed with the FEM would be reflected in a minor underestimation and overestimation of the dyke opening and of the source separation, respectively, while the source deflation would be similar to its reference value.

However, when the discrepancies are of the same order of magnitude in the case of two superposed inflating Mogi sources, we have demonstrated that an inversion based on analytical models, and hence neglecting the source interaction, is not able to retrieve the source parameter(s) unless the source are separated by more than 8 radii.

In this study, we chose a few combinations of deformation sources, of model geometry and physical parameters (Models A–D). Applying the same approach to three case studies based on the magmatic systems of Soufrière Hills Volcano, Montserrat, West Indies (Models CS1 and CS2, similar to Models A and DII, respectively) and of the Dabbahu segment, Afar, Ethiopia (Models CS3, similar to Model DI) gave results in agreement with the theoretical models, showing significant discrepancies for models with superposed magma chambers or with juxtaposed dyke and magma chambers.

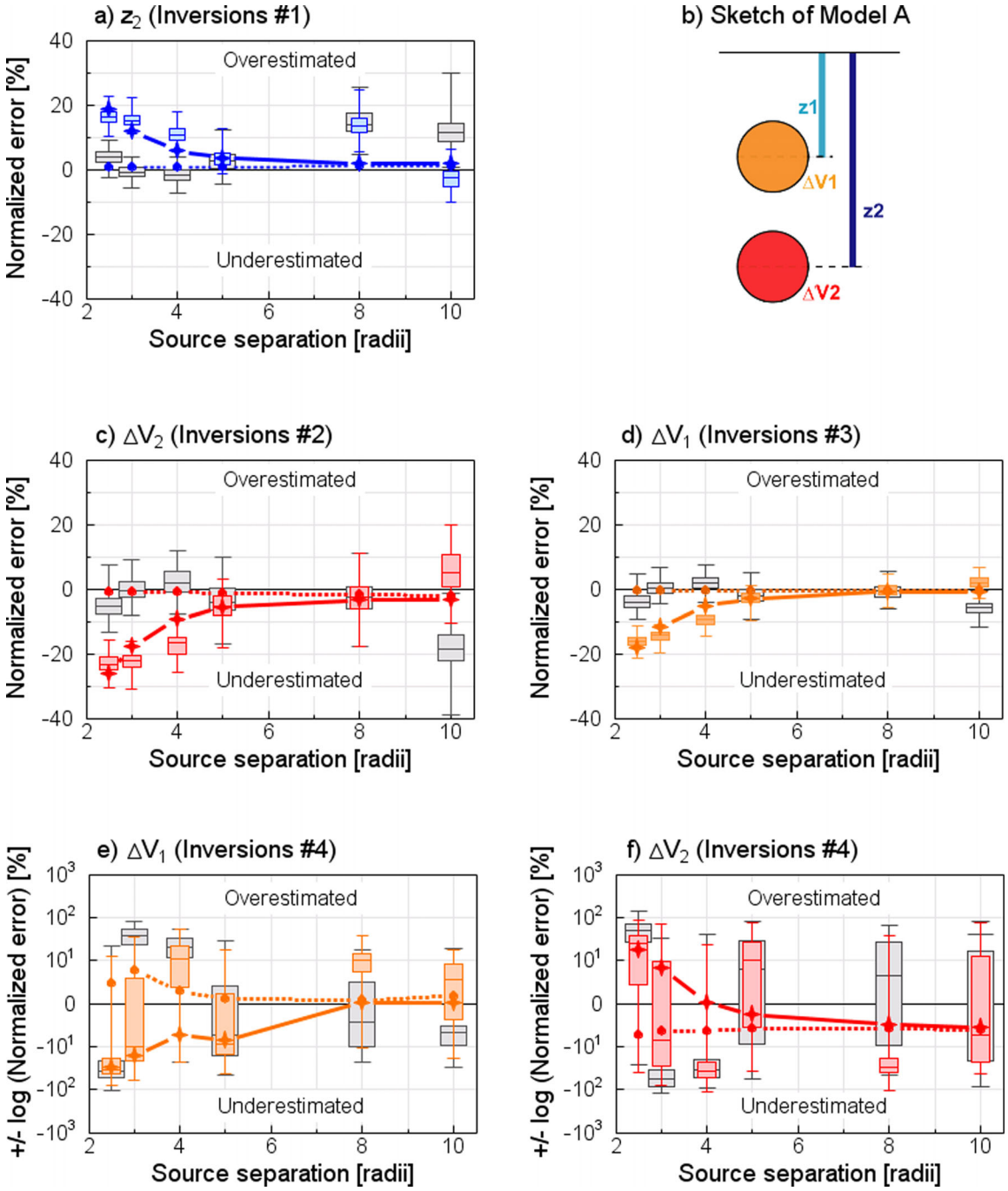

Figure 16. Inversions #1–4: errors between original and retrieved parameters values obtained for a population of 100 inversions of the solution of the synthetic data sets (numerical reference model), using combined analytical models corresponding to Model A-G1'a to f. The reference models consist of two superposed spherical sources of radius $a = 500$ m pressurized by $\Delta P1 = \Delta P2 = 20$ MPa. A Gaussian noise with standard deviation 1 cm has been added to the synthetic solution, which has then been bootstrapped. The population of error between reference and retrieved parameter normalized by the reference parameter is plotted against the reference model source separation. The error distribution obtained for the full FE model and for the 'M1+M2' summed model are indicated in coloured and grey, respectively. The box-and-whiskers plot indicate the minimum, the first quartile, the median, the third quartile and the maximum of the error population. The error obtained for the original synthetic data set are indicated with a solid line for the full FE model and with a dotted line for the 'M1+M2' summed model. The sources are separated by a distance of 2.5, 3, 4, 5, 8 and 9 radii. Inversions #1–#3 retrieve only one parameter at a time: (a) the deeper source depth z_2, (c) the deeper source volume change ΔV_2, (d) the shallower source volume change ΔV_1. (e) and (f) Inversions #4 retrieve both source volume change ΔV_1 and ΔV_2. (b) Sketch of Model A and source parameters inverted for. See also Table 6 for summarized results and the corresponding figure for Inversions #5 (Fig. A-8).

We have demonstrated for several magmatic systems, that the interaction between sources are negligible and the source parameters can be retrieved correctly through an analytical inversion, either due to the nature of the model geometry (i.e. Models C, DII), or because the deformation sources are far enough, or because of the absence of deformation data in the near field. However, in some cases, translating the sources volume change into realistic overpressures, which does not overcome the tensile strength of the surrounding medium

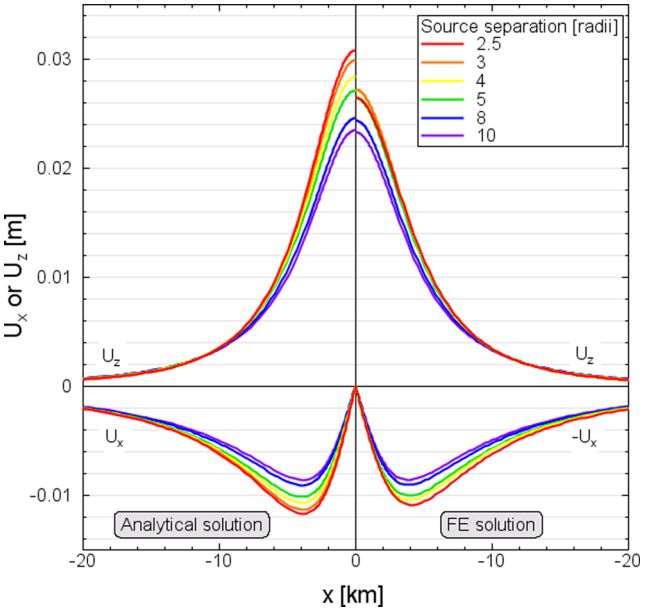

Figure 17. Profiles above the source centre comparing the analytical (left-hand panel) and FE (right-hand panel) vertical and horizontal surface displacements for models with two superposed spherical sources (Model A-G1') for source separations between 2.5 and 10 radii. For easier comparison, we mirrored the horizontal displacements of the FE solution.

(Gudmundsson 2012) might imply, due to the trade-off between pressure change and radius (Delaney & McTigue 1994), the existence of large magma chambers, close enough to interact. Moreover, our results for the analytical inversions of superposed magma chambers (Model A) indicate that deep storage systems are 'intrinsically' indeterminable by means of geodetic data only: when the vertical distance between different magma chambers is small, they interact and the solution is not unique, and when the distance is large, the magma chambers do not interact much, but the signal of the deeper source might become too small to be detected. For magmatic systems with a more complex, finer structure, with two or more storage zones at different depths (i.e. smaller deformation sources within a same magma reservoir, rather than distinct magma chambers, e.g. Sigmundsson *et al.* 2010, on Eyjafjallajokull Volcano, Iceland), it would be difficult, at the very least, to invert for source depth and volume change at once, and independent information on source depth, for example petrological constraints, should be integrated in the procedure.

Additionally, when inverting jointly for all source volume changes and depths, the source interaction but also the noise contamination can make the solution unstable although all source parameters are retrieved within ± 10 per cent beyond the threshold distance of 8 radii.

Finally, this study also shows how the choice of the method to model numerically a dyke or a magma chamber is critical when several sources are combined and located next to each other. The dyke can be made flexible by defining the displacement of one wall relative to the other. While generally magma chambers are modelled as cavities, implying that the magma they contain is fluid, it would be appropriate to model magma chambers more realistically as an inclusion, assigning to the magma at least a finite incompressibility, if not a stiffness when the magma is a solid matrix with melt-filled pores. By treating our deformation sources as cavities, we optimize their capability to interact with each other. In models with neighbouring sources, realistic magma bodies with a rigidity, compressibility and viscosity, will behave in a different fashion than fluid-filled magma bodies. Hence in those cases, numerical models must include realistic magma properties. In this study, we have isolated the effect of source interaction and applied a significance threshold of 5 per cent which we have defined through the calibration of the FE models against the analytical models. For two superposed spherical magma chambers, we have found that the interaction between sources could lead to underestimating the chamber volume change by up to 30 per cent. In the context of more complex modelling approaches, the compressibility of the magma and topography could have an impact of 80 per cent (Johnson *et al.* 2000; Voight *et al.* 2010) and 10–50 per cent (Cayol & Cornet 1998) on the magma chamber volume change, respectively. Medium heterogeneities can introduce discrepancies at the surface of for example 2–40 per cent for Poisson's ratio of 0.21–0.34 (Cayol & Cornet 1998; Masterlark 2007). Depending on the magmatic system studied, several of these factors can be present simultaneously, and evaluating which ones are dominant should be evaluated on a case by case basis.

It is needless to say that numerical modelling has the advantage of simultaneously accounting for complex model geometry and the interaction between several deformation sources. However, we have demonstrated that a combination of analytical models constitutes a valid modelling approach as long as the critical source configuration and separation presented in this study are observed.

ACKNOWLEDGEMENTS

We thank Stefanie Hautmann and an anonymous reviewer for their critical reviews which helped improving the manuscript significantly. We are grateful to Greg Houseman, Tim Wright and several members of the Volcanic Studies Group at the University of Leeds for their constructive comments on an earlier version of the manuscript. We are also indebted to Gilda Currenti (INGV Catania, Italy), Fabio Pulvirenti (University of Catania, Italy) and the Comsol Multiphysics Technical Support staff for their help with some FE modelling aspects of this study. This work has been funded by a NERC studentship, and by the European-funded VUELCO project.

REFERENCES

Abidin, H.Z., Andreas, H. & Gamal, M., 2005. The deformation of Bromo Volcano (Indonesia) as detected by GPS surveys method, *J. Glob. Position. Syst.,* **3**(1-2), 16–24.

Arnadóttir, T., Sigmundsson, F. & Delaney, P.T., 1998. Source of crustal deformation associated with the Krafla, Iceland, eruption of September 1984, *Geophys. Res. Lett.,* **25**(7), 1043–1046.

Ayele, A. *et al.*, 2009. September 2005 mega-dike emplacement in the Manda-Harraro nascent oceanic rift (Afar depression), *Geophys. Res. Lett.,* **36**(20), 1–5.

Bonaccorso, A. & Davis, P.M., 1999. Models of ground deformation from vertical volcanic conduits with application to eruptions of Mount St. Helens and Mount Etna, *J. geophys. Res.,* **104**(B5), 10 531–10 542.

Bonaccorso, A., Gambino, S., Guglielmino, F., Mattia, M., Puglisi, G. & Boschi, E., 2008. Stromboli 2007 eruption: deflation modeling to infer shallow-intermediate plumbing system, *Geophys. Res. Lett.,* **35**(6), L06311.

Cayol, V. & Cornet, F.H., 1998. Effects of topography on the interpretation of the deformation field of prominent volcanoes—application to Etna, *Geophys. Res. Lett.,* **25**(11), 1979–1982.

Clarke, P.J., 1996. Tectonic Motions and Earthquake Deformation in Greece from GPS Measurements, *PhD thesis,* University of Oxford.

Currenti, G., Del Negro, C., Ganci, G. & Scandura, D., 2008. 3D numerical deformation model of the intrusive event forerunning the 2001 Etna eruption, *Phys. Earth planet. Inter.,* **168**(1-2), 88–96.

Davis, P.M., 1983. Surface deformation associated with a dipping hydrofracture, *J. geophys. Res.,* **88**(B7), 5826–5834.

Delaney, P.T. & McTigue, D.F., 1994. Volume of magma accumulation or withdrawal estimated from surface uplift or subsidence, with application to the 1960 collapse of Kilauea volcano, *Bull. Volcanol.,* **56**(6-7), 417–424.

Dragoni, M. & Magnanensi, C., 1989. Displacement and stress produced by a pressurized , spherical magma chamber, surrounded by a viscoelastic shell, *Phys. Earth planet. Inter.,* **56,** 316–328.

Dvorak, J.J. & Dzurisin, D., 1997. Volcano geodesy: the search for magma reservoirs and the formation of eruptive vents, *Rev. Geophys.,* **35**(3), 343–384.

Efron, B. & Tibshirani, R., 1986. Bootstrap methods for standard errors, Confidence intervals, and other measures of statistical accuracy, *Stat. Sci.,* **1**(1), 54–75.

Elsworth, D., Mattioli, G.S., Taron, J., Voight, B. & Herd, R., 2008. Implications of magma transfer between multiple reservoirs on eruption cycling, *Science,* **322**(5899), 246–248.

Fialko, Y., Simons, M. & Khazan, Y., 2001. Finite source modelling of magmatic unrest in Socorro, New Mexico, and Long Valley, California, *Geophys. J. Int.,* **146**(1), 191–200.

Foroozan, R., Elsworth, D., Voight, B. & Mattioli, G.S., 2010. Dual reservoir structure at Soufrière Hills Volcano inferred from continuous GPS observations and heterogeneous elastic modeling, *Geophys. Res. Lett.,* **37**(19), doi:10.1029/2010GL042511.

Gdoutos, E., 1981. Interaction effects between a crack and a circular inclusion, *Fibre Scie. Technol.,* **15**(3), 173–185.

Gorbatikh, L., Lomov, S. & Verpoest, I., 2007. On stress intensity factors of multiple cracks at small distances in 2-D problems, *Int. J. Fract.,* **143**(4), 377–384.

Gottsmann, J., Folch, A. & Rymer, H., 2006. Unrest at Campi Flegrei: a contribution to the magmatic versus hydrothermal debate from inverse and finite element modeling, *J. geophys. Res.,* **111**(B7), B07203, doi:10.1029/2005JB003745.

Grechka, V. & Kachanov, M., 2006. Effective elasticity of rocks with closely spaced and intersecting cracks, *Geophysics,* **71**(3), D85–D91.

Gudmundsson, A., 2012. Magma chambers: formation, local stresses, excess pressures, and compartments, *J. Volc. Geotherm. Res.,* (237–238, 19–41.

Hamling, I.J., Wright, T.J., Calais, E., Bennati, L. & Lewi, E., 2010. Stress transfer 802 between thirteen successive dyke intrusions in Ethiopia, *Nat. Geosci.,* **3**(10), 713–717.

Hughes, G.R., 2011. Reinvestigation of the 1989 Mammoth Mountain, California seismic swarm and dike intrusion, *J. Volc. Geotherm. Res.,* **207**(3-4), 106–112.

Jaeger, J., Cook, N. & Zimmerman, R., 2007. *Fundamentals of Rock Mechanics,* 4th edn, Vol. 470, John Wiley & Sons.

Johnson, D.J., Sigmundsson, F. & Delaney, P.T., 2000. Comment on "Volume of magma accumulation or withdrawal estimated from surface uplift or subsidence, with application to the 1960 collapse of Klauea volcano" by P. T. Delaney and D. F. McTigue, *Bull. Volcanol.,* **61**(7), 491–493.

Kachanov, M., 1987. Elastic solids with many cracks: a simple method of analysis, *Int. J. Solids Struct.,* **23**(1), 23–43.

Kachanov, M., 2003. On the problems of crack interactions and crack coalescence, *Int. J. Fract.,* **120,** 537–543.

Kohno, Y., Matsushima, T. & Shimizu, H., 2008. Pressure sources beneath Unzen Volcano inferred from leveling and GPS data, *J. Volc. Geotherm. Res.,* **175**(1-2), 100–109.

Linde, A.T. *et al.*, 2010. Vulcanian explosion at Soufrière Hills Volcano, Montserrat on March 2004 as revealed by strain data, *Geophys. Res. Lett.,* **37,** 1–5.

Lisowski, M., 2007. Analytical volcano deformation source models, in *Volcano Deformation,* Chap. 8, pp. 279–304, Springer-Verlag.

Long, S.M. & Grosfils, E.B., 2009. Modeling the effect of layered volcanic material on magma reservoir failure and associated deformation, with application to Long Valley caldera, California, *J. Volc. Geotherm. Res.,* **186**(3-4), 349–360.

Lungarini, L., Troise, C., Meo, M. & Denatale, G., 2005. Finite element modelling of topographic effects on elastic ground deformation at Mt. Etna, *J. Volc. Geotherm. Res.,* **144**(1-4), 257–271.

Masterlark, T., 2007. Magma intrusion and deformation predictions: sensitivities to the Mogi assumptions, *J. geophys. Res.,* **112**(B6), 1–17.

McTigue, D.F., 1987. Elastic stress and deformation near a finite spherical magma body: resolution of the point source paradox, *J. geophys. Res.,* **92,** 12 931–12 940.

Mogi, K., 1958. Relations between the eruptions of various volcanoes and the deformations of the ground surfaces around them, *Bull. Earthq. Res. Instit.,* **36,** 99–134.

Montgomery-Brown, E.K., Sinnett, D.K., Poland, M., Segall, P., Orr, T., Zebker, H. & Miklius, A., 2010. Geodetic evidence for en echelon dike emplacement and concurrent slow slip during the June 2007 intrusion and eruption at Kilauea volcano, Hawaii, *J. geophys. Res.,* **115**(B7), 1–15.

Nishimura, T., Ozaway, S., Murakami, M., Sagiya, T., Tada, T., Kaidzu, M. & Ukawa, M., 2001. Crustal deformation caused by magma migration in the northern Izu Islands, Japan, *Geophys. Res. Lett.,* **28**(19), 3745–3748.

Okada, Y., 1985. Surface deformation due to shear and tensile faults in a half-space, *Bull. seism. Soc. Am.,* **75**(4), 1135–1154.

Okada, Y., 1992. Internal deformation due to shear and tensile faults in a half-space, *Bull. seism. Soc. Am.,* **82**(2), 1018–1040.

Palano, M., Puglisi, G. & Gresta, S., 2008. Ground deformation patterns at Mt. Etna from 1993 to 2000 from joint use of InSAR and GPS techniques, *J. Volc. Geotherm. Res.,* **169**(3-4), 99–120.

Piombo, A., Tallarico, A. & Dragoni, M., 2007. Displacement, strain and stress fields due to shear and tensile dislocations in a viscoelastic half-space, *Geophys. J. Int.,* **170**(3), 1399–1417.

Pollard, D.D. & Holzhausen, G., 1979. On the mechanical interaction between a fluid-filled fracture and the Earth's surface, *Tectonophysics,* **53,** 27–57.

Pollard, D.D. & Muller, O.H., 1976. The effect of gradients in regional stress and magma pressure on the form of sheet intrusions in cross section, *J. geophys. Res.,* **81**(5), 975–984.

Pulvirenti, F., Aloisi, M., De Guidi, G. & Mattia, M., 2009. A finite element test of the 2002–2003 Etna eruption, in *Proceedings of the Geoitalia 2009 VII, Italian Forum of Earth Sciences,* September 9–11, 2009, Rimini, Milan, Italy.

Rivalta, E. & Segall, P., 2008. Magma compressibility and the missing source for some dike intrusions, *Geophys. Res. Lett.,* **35**(4), 0–4.

Sanderson, R., Johnson, J. & Lees, J., 2010. Ultra-long period seismic signals and cyclic deflation coincident with eruptions at Santiaguito volcano, Guatemala, *J. Volc. Geotherm. Res.,* **198**(1-2), 35–44.

Sigmundsson, F., Pinel, V., Lund, B., Albino, F., Pagli, C., Geirsson, H. & Sturkell, E., 2010. Climate effects on volcanism: influence on magmatic systems of loading and unloading from ice mass variations, with examples from Iceland., *Phil. Trans. Ser. A: Math., Phys. Eng. Sci.,* **368**(1919), 2519–2534.

Stiros, S.C., Psimoulis, P., Vougioukalakis, G. & Fyticas, M., 2010. Geodetic evidence and modeling of a slow, small-scale inflation episode in the Thera (Santorini) volcano caldera, Aegean Sea, *Tectonophysics,* **494**(3-4), 180–190.

Sturkell, E., 2003. Recent unrest and magma movements at Eyjafjallajökull and Katla volcanoes, Iceland, *J. geophys. Res.,* **108**(B8), 1–13.

Tiampo, K.F., Rundle, J., Fernandez, J. & Langbein, J., 2000. Spherical and ellipsoidal volcanic sources at Long Valley caldera, California, using a genetic algorithm inversion technique, *J. Volc. Geotherm. Res.,* **102**(3-4), 189–206.

Voight, B., Widiwijayanti, C., Mattioli, G.S., Elsworth, D., Hidayat, D. & Strutt, M., 2010. Magma-sponge hypothesis and stratovolcanoes: case for a compressible reservoir and quasi-steady deep influx at Soufrière Hills Volcano, Montserrat, *Geophys. Res. Lett.,* **37,** 0–4.

Williams, C.A. & Wadge, G., 1998. The effects of topography on magma chamber deformation models: application to Mt. Etna and radar interferometry, *Geophys. Res. Lett.,* **25**(10), 1549–1552.

Wright, T.J., Parsons, B., Jackson, J., Haynes, M., Fielding, E., England, P. & Clarke, P.J., 1999. Source parameters of the 1 October 1995 Dinar (Turkey) earthquake from SAR interferometry and seismic bodywave modelling, *Earth planet. Sci. Lett.,* **172**(1-2), 23–37.

Wright, T.J., Ebinger, C., Biggs, J., Ayele, A., Yirgu, G., Keir, D. & Stork, A., 2006. Magma-maintained rift segmentation at continental rupture in the 2005 Afar dyking episode., *Nature,* **442**(7100), 291–4.

Yang, B.Y.X. & Davis, P.M., 1992. Geodetic analysis of dike intrusion and motion of the magma reservoir beneath the summit of Kilauea volcano, Hawaii: 1970-1985, *J. geophys. Res.,* **97,** 3305–3324.

de Zeeuw-van Dalfsen, E., Pedersen, R., Hooper, A. & Sigmundsson, F., 2012. Subsidence of Askja caldera 2000-2009: modelling of deformation processes at an extensional plate boundary, constrained by time series InSAR analysis, *J. Volc. Geotherm. Res.,* **213-214,** 72–82.

SUPPORTING INFORMATION

Additional Supporting Information may be found in the online version of this article:

Table A-1. Models A–D: Description of the geometry and physical parameters of the combined models; Benchmarking results.
Table A-2. Model A: Surface (ϵ) and maximum local (Ξ) discrepancies.
Table A-3. Model B: Surface (ϵ) and maximum local (Ξ) discrepancies.
Table A-4. Model C and Model DII: Surface (ϵ) and maximum local (Ξ) discrepancies.
Table A-5. Model DI, Methods 1–3: Surface (ϵ) and maximum local (Ξ) discrepancies.
Table A-6. Sensitivity analysis of Model A-G1'a and DIa: summary of source parameters minimizing discrepancies between analytical and FE solutions.

Figure A-1. Model DI, Methods 1–3: Surface (ϵ) and maximum local (Ξ) discrepancies obtained for models combining an inflating spherical sphere ($\Delta P = 20$ MPa) and a dyke opening by 1 m.
Figure A-2. Model A (Group G1'): Profile of the surface displacements for source separation of 2.5, 3 and 4 radii.
Figure A-3. Model B (Group G1'): Profile of the surface displacements for source separation of 2.5, 3 and 4 radii.
Figure A-4. Model DI (Method 1): Profile of the surface displacement for source separation of 1.5, 2 and 3 radii.
Figure A-5. Model DI (Method 2–3): Profile of the surface displacement for source separation of 1.5, 2 and 3 radii for models combining an inflating spherical sphere ($\Delta P = 20$ MPa) and a dike opening by 1 m.
Figure A-6. Model DI (Method 2–3): Profile of the surface displacement for source separation of 1.5, 2 and 3 radii for models combining an inflating spherical sphere ($\Delta P = -20$ MPa) and a dike opening by 1 m.
Figure A-7. Model CS1 and CS3: Profiles of the surface displacements (Model CS1) and contourmaps of the horizontal and vertical discrepancies [%] (Model CS3).
Figure A-8. Model A-G1'a to f: analytical Inversions #5 of the synthetic datasets with added random noise and bootstrapped (http://mnras.oxfordjournals.org/lookup/suppl/doi:10.1093/gjiras/ggt343/-/DC1).

Please note: Oxford University Press is not responsible for the content or functionality of any supporting materials supplied by the authors. Any queries (other than missing material) should be directed to the corresponding author for the article.